POLITECNICO DI TORINO
Repository ISTITUZIONALE

A new probabilistic rockfall trajectory model incorporating fragmentation, rock mass quality and block shape variability

Original
A new probabilistic rockfall trajectory model incorporating fragmentation, rock mass quality and block shape variability / Marchelli, M.. - In: INTERNATIONAL JOURNAL OF ROCK MECHANICS AND MINING SCIENCES. - ISSN 1365-1609. - 206:(2026), pp. 1-28. [10.1016/j.ijrmms.2026.106624]

Availability:
This version is available at: 11583/3012937 since: 2026-07-10T10:45:15Z

Publisher:
Elsevier

Published
DOI:10.1016/j.ijrmms.2026.106624

Terms of use:

This article is made available under terms and conditions as specified in the corresponding bibliographic description in the repository

Publisher copyright

(Article begins on next page)

15 November 2026

International Journal of Rock Mechanics & Mining Sciences 206 (2026) 106624

Contents lists available at ScienceDirect

International Journal of Rock Mechanics and Mining Sciences

journal homepage: www.elsevier.com/locate/ijrmms

Research Paper

A new probabilistic rockfall trajectory model incorporating fragmentation, rock mass quality and block shape variability

Maddalena Marchelli

Department of Structural, Geotechnical and Building Engineering (DISEG)- Politecnico di Torino, C.so Duca degli Abruzzi 24, I–10129 Torino, Italy

ARTICLE INFO

Keywords:
Rockfall propagation analysis
Trajectory model
Fragmentation
Rock mass condition
Block shapes

ABSTRACT

Rockfall fragmentation significantly influences the dynamics and hazard footprint of rockfall events, yet it remains poorly represented in most trajectory models. This study presents RockFRAG, a novel probabilistic lumped-mass trajectory model that explicitly incorporates fragmentation processes, block shape variability and rock–mass condition within an experimentally calibrated framework. The fragmentation module accounts for the influence of impact energy, block geometry and structural features, using simplified but physically informed representations of discontinuity orientation, rock–mass quality and block shape to describe their effect on fragmentation likelihood and outcomes. Fragmentation onset is governed by a probabilistic energy-based threshold corrected for shape and discontinuity orientation, while fragment-size distributions and post-impact kinematics are derived from controlled laboratory tests.

As a first assessment, the model is compared against laboratory data, large-scale fragment travel distances, and shape-dependent runout from the Vallirana and Authume field experiments. These preliminary comparisons show that the model captures fragmentation probability, fragment-size statistics and the combined influence of shape and structural quality on runout, offering a robust and computationally efficient tool for simulating fragmentation-driven rockfall dynamics and rockfall hazard analysis.

1. Introduction

Rockfall events represent a significant geohazard in mountainous and engineered slopes, posing risks to infrastructure, human safety, and environmental stability. The dynamics of rockfall phenomena are governed by a complex interplay of geological, geometrical, and mechanical factors. While considerable advancements have been made in delineating detachment zones, physically based numerical modelling of rockfall propagation, and implementing protective measures,[1–3] the fragmentation of falling rock masses, particularly during impact, remains a challenging and often oversimplified aspect in trajectory modelling.[4]

Fragmentation during rockfall can occur through the breakage of intact blocks or disaggregation along pre-existing discontinuities.[5] This process not only alters the number and size of blocks but also significantly affects their post-impact kinematics, energy dissipation, and hazard footprint, i.e. the spatial extent and intensity of the area affected by a rockfall event.[6,7] Despite its critical role, fragmentation is frequently treated as a secondary effect, either as a binary event or through empirical rules, limiting the predictive capability of current rockfall models.

Several modelling frameworks, primarily based on lumped-mass approaches, have attempted to incorporate fragmentation into rockfall simulations, each with varying degrees of physical realism and computational complexity, eventually reverting to spherical contact geometry in non-fragmenting impacts to maintain analytical tractability.

The works of Matas et al.,[8,9] who developed and refined the RockGIS model, can be considered among the most influential. Initially, RockGIS included a fragmentation module based on an arbitrary survival rate,[10] defined as the percentage of blocks that remain intact after impact. Subsequent developments introduced calibration using field data from large-scale rockfall experiments and a parameter that controls scale-variant behaviour.[11] This addition acknowledges that smaller blocks may exhibit greater resistance to breakage than larger ones. In terms of fragment size distribution, the RockGIS framework initially adopted a fractal model,[12] assuming scale invariance in fragmentation behaviour.[10] The model defines the number of initial blocks per unit length, a geometrical factor describing the fractal proportion between the original block and the generated fragments, and a fractal dimension. Later refinements introduced scale-variant behaviour, allowing the fragment size distribution to vary with block size and impact conditions, thereby correcting the limitations of a simple power-law model.[11] Calibration of the geometrical factor used in the fractal fragmentation model was performed using field-scale rockfall tests.

E-mail address: maddalena.marchelli@polito.it.

https://doi.org/10.1016/j.ijrmms.2026.106624
Received 12 February 2026; Received in revised form 17 April 2026; Accepted 26 June 2026
Available online 8 July 2026
1365-1609/© 2026 The Author. Published by Elsevier Ltd. This is an open access article under the CC BY license (http://creativecommons.org/licenses/by/4.0/).

List of abbreviation and symbols

A	Base-10 logarithm of the minimum percentage ratio between the fragment mass and the parent block mass
B	Base-10 logarithm of the percentage ratio between fragment mass and parent block mass at the transition point between the two linear segments of the bilinear distribution of the complementary cumulative distribution of fragments mass
C	Base-10 logarithm of the complementary cumulative probability $1-F$ corresponding to the transition point between the two linear segments of the bilinear distribution of the complementary cumulative distribution of fragments mass
COR_*	Effective restitution coefficient accounting for both rebound and fracture energy dissipation during impact
COR_{n0}	Base restitution coefficient for spherical blocks impacting a given surface perpendicularly
COR_n	Normal coefficient of restitution
COR_t	Tangential coefficient of restitution
D	Base-10 logarithm of the maximum percentage ratio between the fragment mass and the parent block mass
d_{eq}	Equivalent sphere diameter for a given block
k_o	Orientation-dependent coefficient used to modify the tensile strength of a moderately fractured rock mass based on the inclination angle of the discontinuity relative to the impacted surface
k_{s,COR_n}	Coefficient to be applied to COR_{n0} to account for the shape of the block
k_{s,E_th}	Coefficient to be applied to E_{th} to account for the shape of the block
E_{fr}	Energy dissipated during fragmentation, associated with the creation of new fracture surfaces
$E^b_{k_t,n}$	Normal component of the translational kinetic energy at (before) the impact
$E^a_{k_t,n}$	Normal component of the translational kinetic energy after the impact
$E^b_{k_t,t}$	Tangential component of the translational kinetic energy before the impact
$E^a_{k_t,t}$	Tangential component of the translational kinetic energy after the impact
E_{th}	Threshold kinetic energy for the normal component of the translational kinetic energy required to trigger fragmentation, considering the shape and the rock mass condition of the block
m	Mass of the block. The subscript B is used, where necessary, to indicate the parent block
m_f	Mass of a generic fragment. The subscript i may be added to denote the ith fragment, i.e. $m_{f,i}$
m_{th}	Minimum fragment mass threshold, defined as the lower bound mass below which generated fragments are discarded during the Monte Carlo sampling of the fragment-size distribution
n_f	Number of fragments
v^b	Translational velocity before impact. Subscripts B and f are used, where necessary, to indicate the parent block and the fragment, respectively
v^a	Translational velocity after impact. Subscripts B and f are used, where necessary, to indicate the parent block and the fragment, respectively
$\tilde{v^a_f}$	Post-impact velocity vector of the fragment due to normal impact
v^b_n	Normal component of the translational velocity before impact. Subscripts B and f (e.g. $v_{B,n}$, $v_{f,n}$) are used, where necessary, to indicate the parent block and the fragment, respectively
v^a_n	Normal component of the translational velocity before and after impact. Subscripts B and f (e.g. $v_{B,n}$, $v_{f,n}$) are used, where necessary, to indicate the parent block and the fragment, respectively
v^a_t	Tangential component of the translational velocity after impact. Subscripts B and f (e.g. $v_{B,t}$, $v_{f,t}$) are used, where necessary, to indicate the parent block and the fragment, respectively
v_y	yield velocity
V	Volume of the block. The subscript B is used, where necessary, to indicate the parent block
V_{th}	Threshold fragment volume, defined as the volume below which a fragment generated from a moderately fractured rock mass is reclassified as intact
Y_Bs	Secant Young's modulus of the block material
Y_s	Secant Young's modulus of the slope material
Y_{eq}	Local deformation coefficient of the Hertzian contact, function of the block material and the slope material
α	Angle between the normal and tangential components of the post-impact velocity vector of the fragment due to normal impact
ϵ	Ratio between the tangential component of the translational kinetic energy before the impact and the threshold kinetic energy for the normal component of the translational kinetic energy required to trigger fragmentation
θ	Angle of inclination of the joint plane with respect to the impacted surface, used to assess structural control on fragmentation
$\imath$	angle of inclination of the velocity vector at impact with respect to the impacted surface
ν_B	Poisson ratio of the block material
ν_s	Poisson ratio of the slope material
σ_c	Uniaxial compressive strength
σ_t	Tensile strength
$\tilde{\sigma_t}$	Effective tensile strength of the rock mass, accounting for the presence and orientation of discontinuities with respect to the impacted surface
ϕ	Sliding friction angle
ψ	Scaling factor used to normalise the effective restitution coefficient COR_* with respect to the theoretical restitution coefficient COR_e of an elastic–perfectly plastic sphere

Finally, post-impact kinematics were treated in a simplified manner: fragment velocities are assigned stochastically within a cone of arbitrary aperture, and kinetic energy is distributed proportionally to fragment mass. More recently, Gili et al.[13] proposed a functional formulation to describe fragmentation probability, incorporating multiple parameters such as block volume, shape, mechanical resistance, and internal structure, as well as impact energy, incidence angle, and contact geometry. This approach represents a significant advancement over earlier models. However, the mechanical treatment of discontinuities within the rock mass remains empirical. Joint orientation, spacing, and persistence are not explicitly modelled, limiting the ability to simulate structurally controlled fragmentation. Similarly, substrate characteristics, block configuration upon impact, and the five exponents used

in the functional form are difficult to calibrate and may introduce uncertainty in practical applications.

A different approach was proposed by Wang et al.,[14–16] and later extended by Frattini et al.,[17] Dattola et al.,[18] Lanfranconi et al.,[19] within the HY-Stone software.[20] These models define a fragmentation threshold based on a Weibull-type energy criterion,[21] requiring input parameters such as Young's modulus, Poisson's ratio, UCS, block volume, and Weibull constants. While physically grounded, this model is difficult to calibrate in heterogeneous rock masses and do not explicitly account for the presence of discontinuities. Fragment size distributions are typically modelled using power-law relationship, and post-impact velocities are assigned proportionally to fragment mass, with ejection directions stochastically distributed within a user-defined cone.

While computationally efficient, the post-impact approach proposed in both codes does not capture the directional bias or energy partitioning observed in experimental studies. For instance, Marchelli et al.[22] demonstrated that, in controlled drop tests on spherical samples containing one or multiple planar discontinuities at different positions within the specimen, fragment trajectories are strongly influenced by discontinuity orientation and impact angle, with larger fragments tending to follow the normal to the discontinuity plane and smaller fragments exhibiting wider angular dispersion. Similarly, Zhao et al.[23] used a 3D discrete element method to investigate the role of pre-existing joints in rockfall fragmentation, showing that joint orientation and spatial configuration significantly affect both the fragmentation pattern, the rebound energy and the resulting fragment trajectories. These findings challenge the validity of fixed-cone dispersion models and support the need for probabilistic trajectory frameworks that incorporate structural and geometrical controls.

More recently, Guccione et al.[24] proposed a stochastic fragmentation model developed within a lumped-mass rockfall trajectory framework, derived from laboratory drop tests on homogeneous brittle spheres. The model introduces a survival probability function based on the statistical distribution of material properties, offering a physically calibrated criterion for fragmentation. In cases where fragmentation does not occur, the framework allows for the integration of a damage accumulation module to account for the progressive weakening of the block under multiple consecutive impacts. Fragment number and size distributions are derived from experiments and reflect the variability observed in brittle failure under dynamic loading. Accordingly, internal discontinuities are not considered, as the stochastic fragmentation model is calibrated exclusively on laboratory tests involving homogeneous spherical specimens. Referring to the post-impact kinematics, the ratio between normal and tangential components of fragment velocity is extracted from experimental data, allowing the estimation of launch angle and direction. However, the model is restricted to collinear impacts and spherical block geometry, which constrains its applicability in field conditions where block shapes deviate significantly from sphericity and impacts may occur under oblique configurations.

Referring to the fragment size distributions proposed by the aforementioned models, field and laboratory data on intact brittle materials have consistently shown that fragment sizes often follow a power-law distribution.[5,25–27] However, Carmona et al.[28] and Wittel et al.[29] observed that this scaling applies primarily to smaller fragments, while larger ones may conform to Weibull-type distributions, with local maxima linked to meridian crack formation. Despite providing qualitative insight into the governing processes, rather than direct quantitative field-scale characterisation of natural jointed rock masses, recent experimental studies conducted under controlled laboratory conditions suggest that impact-induced fragmentation mechanisms also depend on joint spacing, orientation, block geometry, and impact configuration.[22,30,31]

In contrast to lumped-mass models that attempt to simulate fragmentation, several hybrid,[32,33] rigid-body[34–39] and 3D complex-shaped discrete element trajectory models[40] primarily focus on the influence of block shape and rotational dynamics but, in their standard formulations, do not simulate fragmentation. Three-dimensional numerical approaches including discontinuous deformation analysis (DDA) combined with detailed discontinuity characterisation, have also been used to investigate rockfall failure mechanisms and block kinematics.[41,42] A few recent studies have attempted explicit fragmentation at detailed scale: Wu et al.[43] modelled breakage using the code 3DEC for blocks with prescribed geometry and joint sets, demonstrating feasibility but also reporting high hardware requirements and relatively complex preprocessing and parameter setting. Similarly, Zhang et al.[44] employed a three-dimensional particle-flow code (PFC) approach in which the rock is represented as an assembly of bonded particles and pre-existing joints with assigned properties, and bonds fail when computed tensile or shear stresses exceed their specified maxima, thereby allowing crack initiation and coalescence to emerge. While these methods provide rich physics, they require precise knowledge of block shape and joint locations and are computationally expensive, which confines their use to site-specific studies. For regional hazard assessment or problems with substantial epistemic and aleatory uncertainty,[45] as commonly encountered in rockfall processes, such detailed models are generally impractical.

Taken together, these approaches reveal a clear gap in current modelling capabilities: no existing framework simultaneously accounts for fragmentation, block shape variability, and the mechanical influence of discontinuities. Beyond these modelling strategies, it is important to emphasise that the rockfall processes are inherently probabilistic, as their dynamics are governed by both aleatory and epistemic sources of uncertainty. Aleatory uncertainty reflects the intrinsic variability of the phenomenon, including source location, block geometry, discontinuity arrangement, impact orientation and fragmentation outcome, which leads to significant dispersion of trajectories, impact energies and fragment-size distributions even under apparently identical release conditions. Epistemic uncertainty, by contrast, is related to incomplete knowledge of rock–mass structure, block–slope interaction parameters and initial conditions, which cannot be fully constrained from field surveys or experimental observations. As highlighted by Li and Lan[46] and recent hazard frameworks,[45] deterministic simulations are therefore insufficient to represent the range of physically plausible outcomes. Within this context, probabilistic trajectory modelling based on stochastic sampling techniques (e.g. Monte-Carlo) provides a consistent framework to propagate uncertainty through block propagation and impact fragmentation.

On this basis, the present study introduces a new probabilistic lumped-mass trajectory model, RockFRAG, integrating impact-induced fragmentation and first-order effects of block shape and rock–mass discontinuities unified framework. Its developments is informed by an extensive bibliographic research and by an extensive series of drop tests performed on spherical specimens containing predefined discontinuities,[22] as well as on prismatic and angular samples,[30] providing experimental evidence on impact behaviour, fracture propagation, and fragmentation efficiency across different shapes and structural configurations. The proposed model incorporates:

- a fragmentation module informed by experimental drop tests on differentially jointed spherical samples and irregularly shaped samples;
- probabilistic treatment of block shape and rock mass quality, reflecting natural variability;
- a trajectory engine that simulates fragment motion based on post-impact velocity vectors derived from controlled tests, ensuring a physically consistent representation of fragment kinematics.

To contextualise the proposed approach, Table A.17 in Appendix A compares three existing lumped-mass models (RockGIS, HY-Stone, and NURock) with RockFRAG, highlighting their main attributes and limitations. The proposed framework is presented in three parts: Section 2

describes the probabilistic lumped-mass trajectory model, including a preliminary treatment of block shape and discontinuities. Section 3 details the fragmentation simulation module, informed by experimental data. Section 4 demonstrates the model's application to a real-world scenario, highlighting its predictive capabilities and limitations. Finally, conclusions and future perspectives are outlined in Section 5.

2. Rockfall propagation model framework

The rockfall propagation model presented in this study builds upon a lumped-mass framework implemented in MATLAB.[47] The core equations of the lumped-mass module are conceptually similar to those used in RocFall[48] and to the approach described in Marchelli et al.,[49] both designed to simulate the motion of intact blocks without accounting for shape variability or fragmentation. To ensure robustness and reliability, the lumped-mass module, excluding fragmentation, has been validated using the same methodological principles adopted in Marchelli et al.,[49] without replicating the previously published code. However, the present work introduces a newly developed fragmentation module, while the underlying lumped-mass trajectory approach and its validation follow established methodological principles. Within this approach, as an initial step towards more comprehensive modelling, this module provides a preliminary, physically grounded representation of block shape variability and the presence of discontinuities.

2.1. Model scope, assumption and limitation

The proposed framework adopts a probabilistic lumped-mass trajectory approach, in which rockfall blocks are treated as point masses for trajectory computation, and neither rotational dynamics nor explicit contact geometry are resolved. Block shape and rock–mass structure are therefore not introduced in a geometric or deterministic sense, but are accounted for statistically as effective descriptors influencing fragmentation propensity and fragment-size distributions, rather than trajectory kinematics. This choice reflects the intended application to scenarios characterised by large source areas and substantial epistemic uncertainty. The model currently operates in two dimensions (2D) to balance physical fidelity and computational tractability for Monte Carlo analyses. This choice enables large parametric studies and uncertainty propagation but does not explicitly resolve lateral dispersion or rotational dynamics; a three-dimensional (3D) extension is planned to address these aspects as discussed in the following.

Block geometry is represented through standardised shape classes (e.g., sphere, cube, slab, prism) that are used parametrically in the impact and fragmentation submodels. This approach captures first-order shape effects on contact mechanics and breakage propensity while avoiding the pre-processing burden associated with fully resolved polyhedral geometries. It is also consistent with the shapes investigated in the laboratory tests from which several of the model's empirical formulations were derived.[30]

Rock–mass structure, and hence the presence of discontinuities or joints, is not represented by means of an explicit discontinuity network. Instead, it is represented probabilistically through structural descriptors controlling fragmentation and detachment behaviour. This choice reflects both the lumped-mass formulation and the intended application of the model to spatially extensive and heterogeneous source areas. Rock–mass classification systems such as Rock Mass rating (RMR), Geological Strength Index (GSI), Q-system[50–54] are primarily intended to assess rock-slope stability and overall rock–mass quality, and are not specifically designed to describe rockfall propagation or impact fragmentation processes.[55,56] Accordingly, rock–mass quality is not introduced in the proposed framework through classification indices as direct input parameters, but is accounted for implicitly through the structural descriptors that underpin these classifications, namely fracture intensity, joint spacing and block geometry, which control block detachment mechanisms and the volume and geometry of potentially fragmentable blocks.[57] Three structural classes (intact, moderately fractured, highly fractured), detailed in Section 2.2, are thus adopted to represent ranges of rock–mass conditions in a probabilistic sense, while direct mapping to GSI or RMR remains approximate and is used only for qualitative interpretation (see Section 2.2).

Detailed modelling of crack initiation, propagation, mixed-mode fracture, and explicit discontinuity interaction lies beyond the scope of this work. The adopted assumptions and parameterisations are informed by controlled experiments[22,30] and a synthesis of relevant literature, providing empirical grounding while recognising limits to transferability outside the investigated domains. According to the references and evidence reported in the above-mentioned studies, fragmentation is assumed to be governed primarily by tensile cracking induced by impact-generated stress waves; in jointed blocks, mixed shear–tensile failure modes may occur when discontinuities are inclined with respect to the impact surface, but the onset of breakage remains controlled by the development of tensile stresses.

When fragmentation occurs, the model relies on an energy-based threshold, that depends on tensile strength, which is treated as scale-independent in the present formulation. This assumption is motivated by two complementary considerations. First, rockfall impacts are high-rate dynamic events: typical impact velocities of 5–25 $\mathrm{m\,s^{-1}}$ associated with millisecond-scale contact durations correspond to strain rates on the order of 10^0–$10^4\ \mathrm{s^{-1}}$. Under such conditions, the tensile strength of rock and other quasi-brittle materials exhibits a pronounced rate-dependent increase.[58,59] Differently from the static loading conditions,[60–63] numerical investigations of dynamic fracture further indicate that, above a critical strain rate, classical static size effects based on weakest-link statistics may be significantly reduced or even reversed.[64] In this regime, crack propagation is governed primarily by inertial effects and the activation of multiple interacting fracture planes rather than by the single most critical flaw.[65] Consequently, assuming a size-independent failure stress is physically better justified under dynamic impact loading than in a quasi-static framework. Second, for blocks belonging to the moderately or highly fractured classes, impact-induced failure is predominantly controlled by the orientation, spacing, and persistence of pre-existing discontinuities rather than by the intrinsic tensile strength of the intact matrix.[22,44,66] This structural control is explicitly accounted for through the reduction of tensile strength in the energy-threshold equation (Eq. (2) in Section 4.1), which may reach up to 60% relative to intact values. In such scenarios, any residual size dependence associated with intact-matrix strength becomes secondary to the dominant discontinuity-driven failure mechanism. Thus, since experimental and numerical studies report conflicting trends[60–62] and indicate that the direction and magnitude of size effects in quasi-brittle materials are not intrinsic material properties but emergent features of the governing failure mechanisms, the present model does not explicitly incorporate size-effect laws as formalised in fracture mechanics. Consequently, a potential bias in the estimation of the energy threshold for fragmentation cannot be excluded, which may lead to either an over- or under-prediction of fragmentation likelihood. The introduction of explicit size-effect scaling is therefore recognised as a possible extension of the proposed framework.

After a breakage event, each fragment is propagated as a new block. In the absence of robust data on post-fracture texture and anisotropy,[67,68] fragments inherit the parent shape and material properties as a default assumption. This is a modelling simplification that requires careful qualification depending on the rock–mass class considered. For intact blocks, the assumption is supported by the observation done for angular blocks without pervasive discontinuities, in which fragment shapes tend to resemble those of the parent,[30] and by dynamic fragmentation studies which consistently report that fragments retain the microstructural features of the parent rock, including fracture density, orientation sets and textural anisotropy,[69–71] The well-documented fractal nature of fragment-size distributions in brittle materials further reinforces the expectation that fragments maintain the same fracture

density class as the parent block.[72,73] For moderately fractured blocks, i.e. blocks containing a limited number of visible discontinuities, fragmentation preferentially occurs along those joint planes.[13,22] Pieces produced by separation along a single joint surface are bounded by that surface and, if their volume is smaller than the characteristic in-situ block volume defined by the discontinuity network, they are unlikely to contain further persistent discontinuities.[74] Treating such fragments as still moderately fractured would overestimate the probability of subsequent fragmentation. To address this, the present framework introduces a user-defined threshold volume V_{th}: fragments generated from a moderately fractured parent whose volume falls below V_{th} are reclassified as intact for all subsequent impacts and fragmentation assessments. The default value is set to null (reclassification disabled), when no site-specific joint-spacing data are available. For highly fractured blocks, no analogous volume threshold is introduced (Table 2). In this class, the volumetric joint count indicates a very high fracture density. At this fracture density, any fragment of practically relevant size still intersects multiple discontinuity planes or is itself bounded by several joint surfaces during fragmentation.[5,74] In this context, impact-induced breakage in foliated and anisotropic rocks often preserves the spacing and persistence of foliation-parallel fractures, and field observations on schistose and orthogneiss blocks indicate that fragments inherit the structural fabric and the pre-existing damage network,[66,75] providing additional support for the parent-inheritance assumption across all three structural classes. Accordingly, the inheritance of the highly fractured condition by all generated fragments is retained, which is conservative for hazard assessment purposes.

The fragment-size distribution is calibrated from laboratory drop tests, including configurations with pre-existing discontinuities. These data support empirical distributions (and their energy dependence) suitable for dynamic impacts. Because laboratory campaigns cannot reliably probe scale effects at field block sizes, the resulting distributions have a bounded domain of applicability; extrapolations beyond tested ranges should be treated with caution and, where feasible, bracketed via sensitivity analyses. For intact brittle materials, numerical results by Ma et al.[67] confirm that fragment mass distributions generally follow a power law, widely recognised as characteristic of fully developed fragmentation. Near the damage–fragmentation transition, however, distributions can become bilinear, reflecting a shift from tension-dominated breakup at low velocities to shear-influenced cracking at higher velocities, which produces finer fragments. In the same framework, the power-law exponent (and the associated fractal dimension) increases with impact velocity, and systematic variations of fragment shape descriptors (e.g., elongation and convexity) are observed. Above a threshold, the fragment mass distributions collapse into a unified power-law relationship with a nearly constant exponent, and the distributions of shape descriptors stabilise, indicating that fragment shapes cease their evolution as impact energy further increases. These observations are broadly consistent with the trends captured by the present model, as discussed in Section 3.2.

Beyond the assumptions related to material properties and fragmentation mechanisms, the dimensionality of the numerical framework introduces additional constraints that merit discussion. A further limitation arises from the two-dimensional nature of the model. Fragmentation is a key mechanism driving lateral dispersion of rockfall trajectories; however, in a 2D framework all kinetic energy released during impact-induced breakage is constrained within the modelled profile. In physical three-dimensional conditions, a portion of this energy would be redistributed into out-of-plane motion of the fragments, contributing to lateral spreading and reducing the energy available for downslope propagation. As a result, the 2D formulation may lead to a mild overestimation of longitudinal runout distances for fragmental rockfalls. The model should therefore be interpreted as a physically informed, probabilistic tool that captures the dominant factors of fragmentation-driven propagation, suitable for reproducing first-order runout statistics along the dominant fall direction, with future developments focused on 3D extension, explicit lateral dispersion, and expanded experimental calibration.

Finally, it is worth recalling that as a lumped-mass scheme, several physical effects are embedded in a reduced set of interaction parameters. In particular, the slope-block interaction (e.g., normal and tangential coefficients of restitution) requires site-specific calibration or justified priors. Calibration should, where possible, be performed against non-fragmenting rebounds, and uncertainty in these parameters ought to be accounted for hazard metrics.

Aware of these limitations, using the currently available datasets,[76] which remain particularly scarce with respect to post-impact fragment trajectories and kinematics at field scale, the present study provides a first, pragmatic validation of fragmentation likelihood, fragment-size statistics and runout envelopes. Field-scale tests are intrinsically the most informative for capturing realistic post-impact behaviour, as they integrate complex interactions between block geometry, rock–mass structure, impact configuration and three-dimensional terrain effects; however, such experiments are logistically demanding, costly, and rarely instrumented in sufficient detail to allow exhaustive validation. Within this context, controlled laboratory and large-scale experimental campaigns constitute an essential complementary source of data. Although simplified, they enable systematic control of impact velocity, orientation, block shape and structural configuration, allowing reproducible calibration of fragmentation thresholds, fragment-size distributions and post-impact velocity partitioning. The present work therefore adopts a combined validation strategy, in which controlled experiments are used to constrain key model components, while available field observations are employed to assess consistency at the scale relevant for hazard analysis.

In summary, the proposed framework enables two-dimensional lumped-mass simulations of intact and fragmenting rockfalls, incorporating block-shape effects and rock–mass structural condition in a probabilistic manner to predict fragmentation likelihood, fragment-size distributions and runout envelopes for hazard assessment. The framework does not resolve block rotation or detailed contact geometry; three-dimensional effects and lateral dispersion are neglected in the present study and could be addressed in future developments, while deterministic effects of individual discontinuity sets on block motion are not considered.

2.2. Simulation workflow and initial condition

The simulation workflow begins with the definition of the slope topographic profile and the release conditions of the potentially detachable block, including its initial position and velocity. The block is then characterised in terms of volume V_B, geometry, material density ρ, intact rock mechanical properties (tensile strength σ_t), rock–mass mechanical properties (secant Young's modulus Y and Poisson's ratio ν), and structural condition. Block–slope surface interaction during impacts is described through the normal and tangential coefficients of restitution (COR_n, COR_t), defined as the ratio between the post-impact (after) velocity v^a and the pre-impact (before) velocity v^b along the normal (subscript n) and tangential (subscript t) directions with respect to the local slope surface at the contact point, as detailed in Section 2.3. For motion phases involving contact with the slope, the slope surface–block friction coefficient ($\tan\phi$) represents the primary parameter governing sliding kinematics. These interaction parameters are employed consistently in both fragmentation and non-fragmentation cases to estimate rebound behaviour and the associated energy partitioning, and are assigned based on the types of substrate present in the slope profile. They are described using Gaussian distributions, as commonly adopted in rockfall trajectory modelling for block volumes and block–slope interaction parameters.[46,77] All block-, slope- and fragmentation-related input parameters required by the model are summarised Table 1, together with their physical meaning.

Table 1
Input parameters of the fragmentation module. Parameters treated probabilistically are defined by their mean value and standard deviation used for Monte Carlo sampling.

Category	Symbol	Description	Statistical definition
Block geometry and structure	V_B	Volume of the parent block (m^3)	Mean μ_{V_B}, Std. dev. σ_{V_B}
	Shape	Block shape class (sphere, cube, slab, prism)	Categorical input
	Rock mass condition	Structural condition (intact, moderately fractured, highly fractured)	Categorical input
Block material	ρ	Density ($kg\,m^{-3}$)	Mean μ_ρ, Std. dev. σ_ρ
	σ_t	Tensile strength of intact block material (MPa)	Mean μ_{σ_t}, Std. dev. σ_{σ_t}
	Y_B	Young's modulus of block material (MPa)	Mean μ_{Y_B}, Std. dev. σ_{Y_B}
	ν_B	Poisson's ratio of block material (–)	Mean μ_{ν_B}, Std. dev. σ_{ν_B}
Block release conditions	x_0, y_0	Initial block position (m)	Deterministic
	$v_{x,0}$, $v_{y,0}$	Initial block velocity ($m\,s^{-1}$)	Mean $\mu_{v_{x,0}}$, Std. dev. $\sigma_{v_{x,0}}$, Mean $\mu_{v_{y,0}}$, Std. dev. $\sigma_{v_{y,0}}$
Block fragments threshold	m_{th}	Minimum fragment mass threshold (kg)	Deterministic
	V_{th}	Threshold fragment volume (m^3)	Deterministic
Slope material	Y_s	Young's modulus of slope material (MPa)	Mean μ_{Y_s}, Std. dev. σ_{Y_s}
	ν_s	Poisson's ratio of slope material (–)	Mean μ_{ν_s}, Std. dev. σ_{ν_s}
Block–slope interaction parameters	COR_{n0}	Normal restitution coefficient (base value) (–)	Mean $\mu_{COR_{n0}}$, Std. dev. $\sigma_{COR_{n0}}$
	COR_t	Tangential restitution coefficient (–)	Mean μ_{COR_t}, Std. dev. σ_{COR_t}

With specific reference to the rock mass structural condition, three classes are identified based on fracture intensity and structural integrity as stated in Section 2.1: (i) intact rock, characterised by the absence of visible discontinuities and behaving as a homogeneous brittle material; (ii) moderately fractured rock mass, where a limited number of discontinuities are present, influencing strength and fragmentation behaviour without causing pervasive weakness; and (iii) highly fractured rock mass, defined by a high fracture density or foliation, resulting in markedly reduced tensile strength and a strong predisposition to breakage upon impact. These categories are used throughout the fragmentation module. Although rock–mass quality indices such as GSI, depending on both structural characteristics (blockiness) and discontinuity surface conditions,[78,79] are not used as direct inputs in the proposed framework, structural descriptors such as volumetric joint count J_v and the mean discontinuity spacing, can be used to derive indicative GSI values when required Hoek and Brown.[80] Recent quantification approaches have shown that the structure rating (SR) of the GSI chart[81] can be objectively related to volumetric fracture measures.[82–85] Accordingly, the correspondence reported in Table 2 is provided for qualitative interpretation only and should not be regarded as a deterministic conversion. The structural classes adopted in this model can thus be qualitatively related to indicative ranges of structure rating in the GSI chart and associated descriptors from the literature, as summarised in Table 2. Once GSI is estimated, empirical correlations collected by Russo and Hormazábal[86] can be applied to relate GSI to RMR or other classification systems when needed, while the uncertainty in RMR and GSI assessments highlighted by Abbas et al.[87] reinforces that these correlations are intended for qualitative interpretation only.

The model proceeds through a series of modules, each representing a distinct phase of the rockfall process (Fig. 1). The modular structure of the code was chosen to allow for flexible integration of new experimental findings and calibration parameters.

After an initial evaluation whether, when released, the block slides or comes to rest, if neither condition is met, it is assumed to enter a free-flight motion phase along a parabolic trajectory. This decision is based on the velocity components, slope inclination, and frictional resistance, governed by the friction angle (ϕ). Every time the free-flight trajectory

Table 2
Indicative correspondence between rock mass condition classes adopted in the model and GSI-structure rating (SR), Volumetric joint counts J_v and mean spacing ranges, based on literature anchors. Values are approximate and for qualitative interpretation only.

Rock mass condition	SR range	Typical J_v (joints/m^3)	Mean spacing (m)
Intact or massive	>75	~1	~3.0
Moderately fractured	35–75	~3–15	~0.1–0.5
Highly fractured	<35	~30	~0.01–0.1

of the centre of mass of the block reaches the slope surface, the code performs a sequence of checks:

- fragmentation check based on an energy threshold criterion that accounts for block shape, the presence and orientation of discontinuities (Section 3.1). If fragmentation occurs, the fragmentation module evaluates:
  - the number and the mass of generated fragments, n_f and m_f through Monte Carlo sampling from an empirical cumulative distribution function (ECDF) (Section 3.2);
  - the energy dissipated during breakage, including fracture energy, accounting for the creation of new fracture surfaces and integrating it into the post-impact energy balance (Section 3.3);
  - the post-impact trajectories of each fragment are computed from velocity vectors derived from a physically-based energy balance (Section 3.3);
- if fragmentation does not occur, the model computes the post-impact velocity components of the entire block and, based on these, determines whether the block rebounds, slides, or comes to rest;
- trajectory update: depending on the outcome, every mass still in movement (either the block or its fragments) enter a new motion phase (sliding, free-flight, or rest), according to the post-impact velocity components.

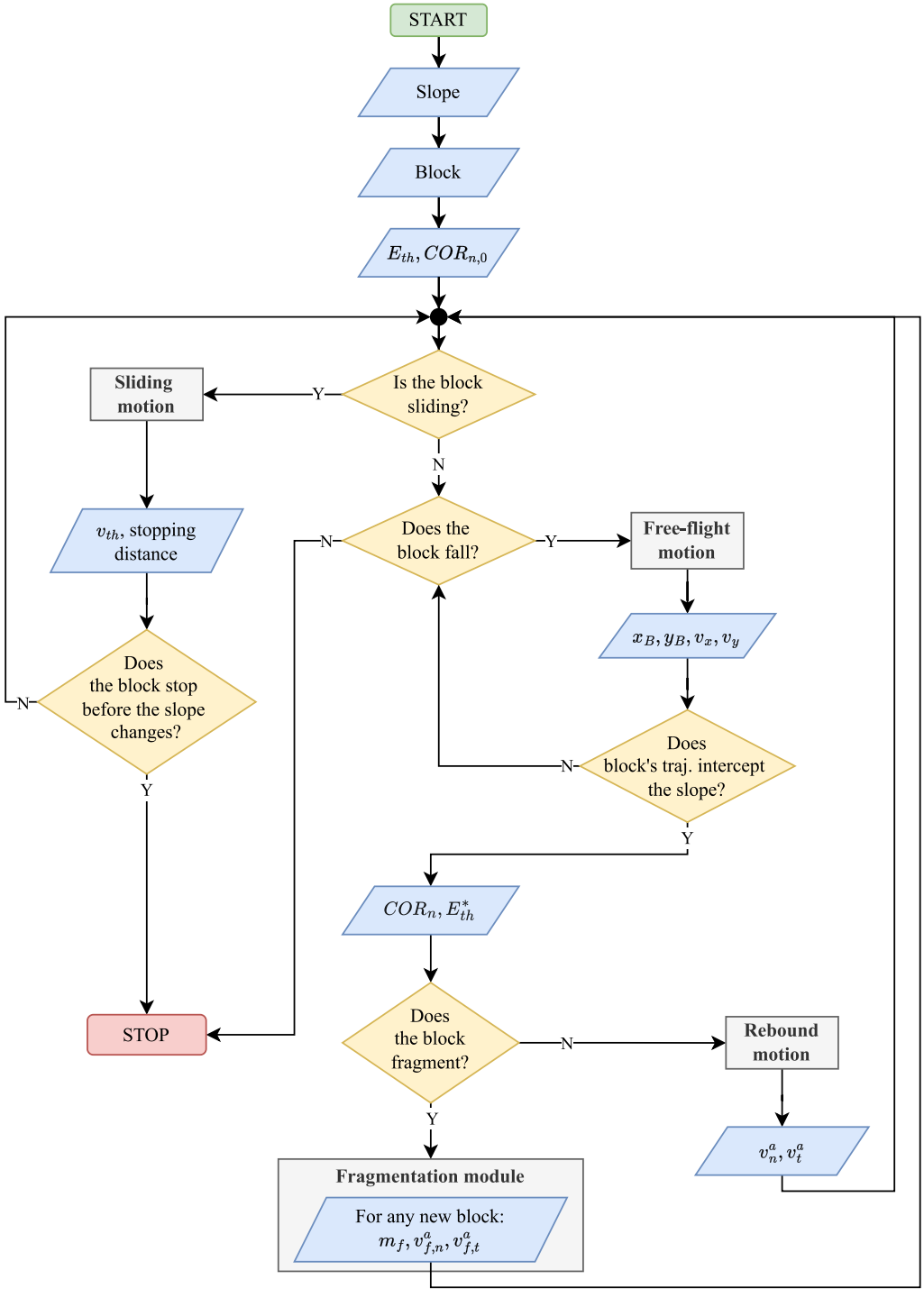


Fig. 1. Workflow of the rockfall propagation model considering fragmentation. To avoid cluttering the notation, subscripts B (block) and f (fragment) have been omitted. The flowchart applies recursively to each fragment, which is treated as a new block in subsequent iterations. For fragments generated from a moderately fractured parent, a reclassification step is applied: if the fragment volume is smaller than the user-defined threshold V_{th}, the fragment is reclassified as intact for all subsequent fragmentation assessments. For intact and highly fractured fragments, mechanical properties of the parent block are inherited.

Fig. 1 presents the flowchart of the entire propagation model, while Fig. 2 details the fragmentation module. The mechanical aspects involved in each step are detailed in the referenced sections, along with the steps for the calibration of the parameters.

All the interactions between the block, its fragments and the slope, in terms of incoming and rebound velocities and block masses are recorded. Each fragment inherits a subset of the parent block's properties, including discontinuity patterns and velocity components, which

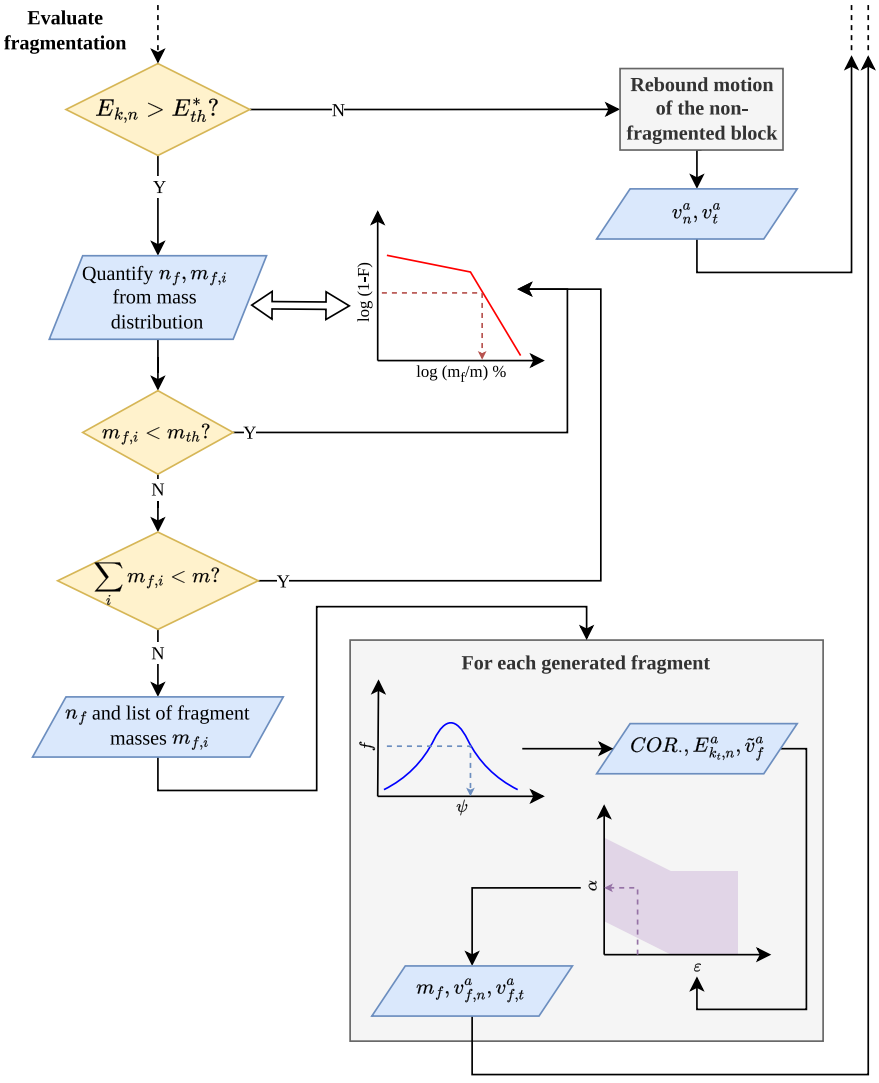


Fig. 2. Flowchart of the fragmentation module within the rockfall propagation model. The diagram outlines the sequence of operations performed when fragmentation is triggered, including threshold evaluation, fragment mass sampling, energy dissipation calculation, and post-impact trajectory assignment.

are then used in subsequent iterations of fragmentation assessment and motion analysis. Regarding structural condition, intact and highly fractured fragments retain the rock–mass class of the parent block, while for moderately fractured fragments, a reclassification step is applied as reported in Section 2.1. This recursive structure allows the model to simulate multi-impact scenarios and progressive fragmentation.

2.3. Selection of the coefficient of restitution

The normal and tangential coefficients of restitution (COR_n, COR_t), or simply COR when referring to the general ratio between post-impact and pre-impact velocity, are fundamental parameters in rockfall trajectory modelling, as they quantify the energy retained after a block–slope surface collision. Their values are influenced by a combination of mechanical, geometrical, and kinematic factors, including substrate type, impact angle, block shape, and velocity.

A comprehensive understanding of these dependencies is essential for accurate simulation of rebound behaviour and energy dissipation. First, the nature of the impacted surface plays a dominant role. Asteriou and Tsiambaos,[88] Ji et al.,[89] Yang et al.[90] and Bi et al.[91] demonstrated that smooth, rigid substrates yield significantly higher COR values than rough or deformable surfaces, with low-angle impacts on smooth surfaces occasionally producing $COR_n > 1$ due to rotational amplification.[92] Impact velocity also influences the dissipation of energy at the block–slope surface collision particularly through its effect on contact duration and deformation. Asteriou and Tsiambaos[88] and Li et al.[93] reported that higher impact velocities tend to reduce COR due to increased plastic deformation and substrate penetration. However, this effect is often secondary to surface and shape influences. Recent experimental work by Marchelli et al.[30] further supports the need for shape-dependent restitution modelling. Drop tests on spheres, cubes, prisms, and slabs showed that compact shapes exhibit higher COR_n values than elongated or flat shapes, with the velocity dependence varying as a function of shape angularity, suggesting that velocity-dependent effects may be shape-specific. Block shape strongly affects impact dynamics: spherical blocks undergoing predominantly collinear impacts tend to exhibit more predictable rebound trajectories and higher coefficients of restitution (COR), whereas angular or elongated blocks experience complex multi-contact interactions, leading to longer impact durations, increased energy dissipation, and lower apparent restitution coefficients.[30,94,95] To account for this, Ji et al.[96] and Bi and Han[97] have introduced a shape factor in the COR_n formulation, quantifying deviation from spherical geometry. Impact angle is another critical variable: multiple studies[89,96,98–100] have shown that COR_n generally decreases with increasing impact angle, particularly in near-perpendicular collisions where energy dissipation is maximised.

Particularly[89] observed that this decay follows a power-law trend, while Tang et al.[100] confirmed a strong negative correlation between COR_n and impact angle. Although these studies do not explicitly propose a cosine function, many trajectory models use it to approximate angular dependence due to its smooth behaviour and ease of calibration. In addition to impact angle and velocity, block mass has been shown to exert a measurable influence on the coefficient of restitution, particularly in impacts involving deformable substrates. Heavier blocks induce greater contact forces and longer interaction durations, which enhance substrate deformation and energy dissipation.[89,90] Asteriou[99] observed that increased block mass correlates with reduced COR_n values, especially on granular or low-stiffness surfaces.

Considering the tangential coefficient of restitution (COR_t) alone, it exhibits minimal dependence on incidence angle, impact velocity, or impacting mass and shape, and is primarily governed by the material properties of the slope surface, such as roughness and stiffness.[90,99]

Summing up all these findings, the model herein proposed allows considering the normal coefficient of restitution (COR_n) as a function of block shape, impact angle, velocity, mass, and substrate properties. While compact empirical formulations accounting for some of these aspects have been proposed in the literature,[89,90,100] the model adopts a flexible structure that allows calibration based on experimental data and site-specific conditions. The proposed formulation, informed by literature and experimental results, is:

$$COR_n = COR_{n0} \cdot k_{s,COR_n} \cdot s_1 \iota^{-s_2} \cdot v_n^{-p} \cdot m^{-q}, \tag{1}$$

where COR_{n0} is the base restitution coefficient for spherical blocks impacting a given surface perpendicularly, and is a function of the mechanical properties of both the block and the slope material. The term k_{s,COR_n} is a shape factor quantifying deviation from spherical geometry. Taking as an example the drop tests by Marchelli et al.,[30] a shape factor of $k_{s,COR_n} \approx 0.85$ for cubes, ≈ 0.5 for slab-like blocks, and ≈ 0.4 for prism-like shapes is suggested. The term ι represents the impact angle (in radians), v_n is the normal component of the impact velocity, and m is the block mass. The coefficient s_1 and the exponents s_2, p and q are calibration constants derived from experimental data. Recent tests, conducted with block masses of approximately 0.1 to 10 kg and impact velocities in the range of about 3–13 m/s, suggest that variations in mass and velocity tend to have a relatively minor influence on COR_n, typically leading to deviations on the order of ±10% from baseline values under otherwise comparable impact conditions.[89,90] Thus, p and q may be approximated as near-zero in preliminary simulations. In contrast, impact angle exerts a strong influence, with variations in COR_n approaching 100% across the angular spectrum,[89,99,100] with typical values of $s_1 > 1$ and $s_2 < 1$.[89,90] To facilitate reproducibility and comparison with future studies, Table 3 reports recommended ranges of benchmark values for the parameters entering Eq. (1). The proposed ranges account for substrate-dependent variability and are consistent with experimental and numerical rockfall studies documenting systematic influences of impact velocity, block mass and ground stiffness on the normal coefficient of restitution. These values are intended as reference benchmarks rather than universal constants, and site-specific calibration is recommended whenever impact test data or back-analysed rockfall events are available. The multiplicative structure of Eq. (1) reflects the combined influence of geometry and kinematics, allowing for flexible calibration across different block shapes, impact scenarios, and substrate conditions. In the code implementation, a flexible structure is provided, enabling users to define COR_n either as a function of multiple parameters or as a value based solely on material properties (i.e., COR_{n0}).

On the contrary, COR_t is assumed to depend only on the material characteristics of the slope surface (e.g., hardness, roughness).

In the proposed model, COR_n and COR_t are used both to estimate rebound velocities in non-fragmentation cases and also to initialise fragment trajectories when breakage occurs (Section 3.3). As rotational velocity is not explicitly considered in the present model, both restitution coefficients are conservatively limited to a maximum value of one and should be calibrated accordingly to encompass this assumption. For both COR_{n0} and COR_t, the values are sampled at each contact using a Monte Carlo technique from a Gaussian distribution, with the mean and standard deviation assigned by the user for each substrate type.

3. Fragmentation simulation module

3.1. Fragmentation threshold

The fragmentation module is the core of the propagation code. Such phenomenon is triggered when the impact energy exceeds a threshold that depends on block and impacted surface material properties, with additional terms to account for block shape and structural features. This approach is conceptually similar to the framework proposed by Lanfranconi et al.,[19] which adopted an earlier energy-based criterion from Yashima et al.,[21] albeit without shape, fractures presence, and orientation corrections. Numerical studies by Ma et al.[67] on the impact fragmentation of quasi-brittle spheres, even in the absence of evident discontinuities, indicate the existence of an intrinsic fracture energy linked to an elastic energy threshold required to break bonds at the microscale. In a complementary work, Ma et al.[106] emphasise the role of a critical energy release rate for modelling fracture growth and crack opening, reinforcing the need to incorporate microscale fracture mechanics into impact-based criteria.

In the present code, the fragmentation originates from the normal motion of the mass against the impacted surface. Its formulation is based on the energy criterion proposed by Tavares and King,[107] which describes the minimum energy required to initiate fracture in a single particle under impact loading. The threshold energy E_{th} is expressed as:

$$E_{\text{th}} = \tilde{\sigma}_t^{5/3} Y_{\text{eq}}^{-2/3} d_{\text{eq}}^3 k_{s,E_{th}}, \tag{2}$$

where $\tilde{\sigma}_t$ is the effective tensile strength of the material, d_{eq} is the equivalent diameter, and Y_{eq} is the local deformation coefficient of the Hertzian contact, which depends on Young's moduli of the block and the impacted surface (Y_B and Y_s, respectively), and their Poisson coefficients (ν_B and ν_s), according to:

$$Y_{\text{eq}} = \frac{Y_B Y_s}{Y_B(1-\nu_s^2) + Y_s(1-\nu_B^2)}. \tag{3}$$

The term $k_{s,E_{th}}$ is a single shape coefficient accounting for the influence of block geometry on the fragmentation threshold energy, as discussed below in the present section.

Although Eq. (2) contains the term d_{eq}^3, which provides a purely geometrical scaling of fracture energy with block volume, the failure stress entering the criterion is treated as scale-independent; the rationale for this assumption is discussed in Section 2.1. As observed by Tavares and King,[107] the influence of loading rate on fracture energy under impact conditions is considered negligible and is therefore not incorporated into the formulation. This assumption does not contradict the observed rate dependence of tensile strength, as the present formulation treats fracture energy as rate-insensitive and adopts a single tensile strength representative of impact loading conditions, without explicitly modelling strain-rate effects.

The expression in Eq. (2) assumes homogeneous, isotropic material behaviour and spherical geometry. However, field and laboratory studies have shown that this assumption may not hold in jointed or foliated rock masses. In particular,Giacomini et al.[66] demonstrated that fragmentation can occur at significantly lower energies in rocks with high discontinuity density. In such cases, the orientation of discontinuities relative to the impact surface becomes the dominant factor controlling fragmentation, as highlighted by the experimental campaign conducted by Marchelli et al.[22] and the numerical results of Zhao et al.[23] To account for such outcomes, the effective tensile strength $\tilde{\sigma}_t$ is a fraction

Table 3
Recommended ranges of benchmark values for the parameters controlling the normal coefficient of restitution in Eq. (1).

Parameter	Substrate/condition	Recommended range	Representative references
COR_{n0}	Hard rock/concrete	0.55–0.75	
	Weathered rock/stiff soil	0.40–0.60	Asteriou et al.,[101] Giani,[75] Bi and Han[97] and RocScience Inc.[48]
	Soft soil/debris	0.20–0.40	
p (velocity exponent)	–	≤0.02	Asteriou and Tsiambaos,[88] Ji et al.[89] and Bi and Han[97]
q (mass exponent)	–	≤0.04	Asteriou and Tsiambaos,[88] Ji et al.,[89] Wang et al.[102] and Bi and Han[97]
s_1; s_2 (inclination coefficients)	–	1–1.2; 0.145–0.195	Ji et al.,[89] Asteriou[99] and Tang et al.[100]
k_{s,COR_n} (shape coefficient)	Cube-like	0.65–0.85	
	Slab-like	0.5–0.68	Das and Cleary,[103] Ji et al.,[89] Marchelli et al.,[104] Qin et al.[105] and Bi and Han[97]
	Prism-like	0.40–0.65	
	Triangular-like	0.4–0.5	

of its nominal value obtained from an intact rock, namely σ_t. Three scenarios are considered on the bases of the structural condition of the rock mass.

1. Intact rock: the tensile strength remains unmodified, i.e. $\tilde{\sigma} = \sigma_t$.
2. Moderately jointed rock mass: in the presence of discontinuities, an orientation-dependent coefficient k_o is introduced to modify the tensile strength. Following the findings of Ma et al.[108] and Han et al.,[109] the corrected tensile strength $\tilde{\sigma}_t$ is defined as:
   - $\tilde{\sigma}_t \approx 0.5\sigma_t$ when the discontinuity is perpendicular to the loading axis ($\theta = 90°$),
   - $\tilde{\sigma}_t \approx \sigma_t$ for orientations parallel or up to 50° to the loading axis.

   For intermediate orientations, the tensile strength correction is not applied through a linear interpolation, but rather follows the trend proposed by Han et al.,[109] which best fits the single plane of weakness theory described by Lee and Pietruszczak.[110]
3. Highly fractured rock mass: a conservative reduction of 60% is assumed, i.e. $\tilde{\sigma}_t \approx 0.4\sigma_t$, as suggested by Zhou et al.[111]

These three rock mass conditions are also used to derive subsequent fragmentation parameters, including the fragment mass distribution, the energy dissipated during breakage, and the post-impact trajectories of the resulting fragments.

Since the orientation of discontinuities relative to the impact surface is unknown in a lumped-mass approach, a probabilistic Monte Carlo sampling technique is applied at each impact for the case of a moderately jointed rock mass, reflecting the natural variability in joint orientation and enabling the model to simulate structurally controlled fragmentation without requiring explicit geometric resolution.

Block shape effects are incorporated through the shape coefficient $k_{s,E_{th}}$, which modifies the fragmentation threshold energy to account for geometric influences on impact-induced failure.[30,103,112] In the proposed framework, block shape is provided to the code as a categorical input by assigning each block to one of four simplified shape classes, namely sphere, cube, slab-like or prismatic. This discretisation is consistent with the lumped-mass formulation and is informed by the comparative experimental analysis of angular blocks presented in Marchelli et al.,[30] which demonstrated systematic differences in fragmentation propensity and energy dissipation among these geometries. Accordingly, typical values of the shape coefficient are adopted as

$$k_{s,E_{th}} = \begin{cases} 2.0, & \text{cube}, \\ 1.7, & \text{slab-like shape}, \\ 1.5, & \text{prismatic block}, \end{cases} \tag{4}$$

reflecting the increasing susceptibility to fragmentation relative to spherical geometry. These values are automatically assigned once the shape class is selected, but may be freely modified for alternative calibrations or site-specific conditions. When quantitative geometric information is available, shape class assignment can be performed objectively prior to simulation using elongation, flatness and compactness indices,[113] or sphericity,[89] providing a reproducible mapping between real block geometries and the adopted shape classes

For each impact the ratio ϵ between the normal component of impact energy, $E^b_{k_t,n}$, and the fragmentation threshold energy is computed as:

$$\epsilon = \frac{E^b_{k_t,n}}{E_{\text{th}}}. \tag{5}$$

Fragmentation occurs if $\epsilon > 1$.

This hybrid approach integrates deterministic fracture mechanics with probabilistic structural controls, consistent with the survival-probability framework of Guccione et al.,[24] thereby improving the physical realism of fragmentation modelling in jointed rock masses. It should be recalled that in subsequent fragmentation events, shape and material properties are inherited from the parent block for all structural classes. The structural class is also inherited, with the exception for moderately fracture blocks as detailed in Section 2.1.

3.2. Fragments number and size distribution

The number and size distribution of fragments upon fragmentation are determined through a probabilistic approach that accounts for the three basic rock conditions, i.e. intact or fractured rock masses. For intact blocks, the adopted formulation is based on the experimental results of Guccione et al.,[114] while for moderately to highly fractured rock masses, the model relies on the findings of Marchelli et al.[22] Both datasets were acquired from drop tests on spherical specimens (100 mm diameter), conducted under controlled conditions with impacts normal to the slope surface and negligible rotational velocities. These settings ensured consistency in the derivation of fragmentation parameters. In both references, the tests revealed that the logarithm (base 10) of the ratio between fragment mass and initial block mass, $\log_{10}(m_f/m)$, against the logarithm of the complementary cumulative distribution of fragment masses, $\log_{10}(1-F)$, yields a bilinear trend.

Fig. 3 illustrates a representative bilinear distribution, where:

- coordinate A corresponds to the base-10 logarithm of the minimum percentage ratio between the fragment mass and the parent block mass,
- coordinates B and C represent the $\log_{10}(m_f/m)$ in percent and $\log_{10}(1-F)$ values at the transition between the two linear trends,
- coordinate D denotes the $\log_{10}(m_f/m)$ (in percent) of the largest fragment.

In the absence of fragmentation, A equals zero, B and D coincide at a value of 2, and C equals zero. For all cases, A has been fixed at −1, i.e., $m_f/m = 0.001$ (i.e., 0.1% of the fragmenting mass), representing the minimum fragment size considered in the analysis.

The slope of the two linear segments, as well as the location of the transition point between them, are found to depend primarily on two factors: (i) the fracture density of the specimen, and (ii) the impact velocity, which reflects the energy input. Based on the experimental results, specimens with a single discontinuity are considered

Table 4
Fitting equations for bilinear parameters B, C, and D as functions of the energy ratio ϵ, for intact, moderately and highly fractured rock masses. A is equal to −1. The coefficient R^2 is reported for each fit.

Rock mass condition	B	C	D
Intact	$2.293e^{-0.334(\epsilon-1)} - 0.293$ ($R^2 = 0.92$)	$0.645e^{-0.341(\epsilon-1)} - 0.645$ ($R^2 = 0.96$)	$0.742e^{-0.629(\epsilon-1)} + 1.276$ ($R^2 = 0.99$)
Moderately fractured	$0.622e^{-6.501(\epsilon-1)} + 1.398$ ($R^2 = 0.98$)	$0.855e^{-10.88(\epsilon-1)} - 0.855$ ($R^2 = 0.94$)	$0.289e^{-5.820(\epsilon-1)} + 1.711$ ($R^2 = 0.98$)
Highly fractured	$1.392e^{-0.831(\epsilon-1)} + 0.608$ ($R^2 = 0.95$)	$0.482e^{-0.497(\epsilon-1)} - 0.482$ ($R^2 = 0.98$)	$0.103e^{-0.562(\epsilon-1)} + 1.897$ ($R^2 = 0.98$)

representative of a moderately jointed rock mass, whereas those with three discontinuities are used to simulate highly fractured conditions. The data were grouped into these two categories, and within each category, further subdivided according to impact velocity. Although joint orientation at impact does influence fragmentation behaviour, its variability was found to be less significant than that of fracture density and velocity. Therefore, for each category and velocity range, the values of B, C, and D were determined by taking the median across all the experimentally tested orientations.

A regression analysis was subsequently performed to derive best-fit equations for the bilinear parameters B, C, and D as functions ϵ. As the laboratory tests were conducted under vertical drop conditions, the normal component of impact velocity was selected for this ratio, ensuring consistency with the experimental setup. This formulation enables the use of these equations during trajectory analysis as a function of the energy ratio, independently of block mass, thereby enhancing model generality. Nevertheless, the validity of the fitted expressions remains confined to the investigated domain, specifically up to $\epsilon \approx 7.86$ for intact rock, $\epsilon \approx 3.12$ for moderately fractured rock masses, and $\epsilon \approx 5.95$ for highly fractured ones. In the case of moderately fractured specimens, where the fragmentation threshold depends on the orientation of the discontinuity plane relative to the impacted surface, the value corresponding to the highest E_{th}, i.e. $\theta = 0°$, was conservatively adopted to ensure safety in predictive applications. These fitted expressions are employed to define the complementary cumulative distribution curve of fragment masses (Table 4) in the validated range. The values of B, C and D outside the range are determined from the proposed equations, as well. For $\epsilon \to \infty$, B converges to −0.293, 1.398, 0.972, C to −0.645, −0.855,−0.482 and D to 1.276, 1.711, 1.897, for intact, moderately and highly fractured rock mass, respectively.

Through Monte Carlo technique, fragment masses are sampled. Specifically, random values of $\log_{10}(1 - F)$ in the range $(-2; 0)$ are extracted and the corresponding m_f/m derived from the selected bilinear curve are determined. The extraction process continues until the cumulative mass of the generated fragments equals the block mass before fragmentation, ensuring mass conservation across fragmentation events. To avoid the generation of excessively small fragments and the associated computational burden, a minimum threshold mass m_{th} is defined. If a sampled fragment mass falls below this threshold, it is discarded and the sampling process continues until the total mass of accepted fragments matches the initial block mass.

3.3. Fragments motion

The post-impact motion of fragments is described through a physically-based energy balance, calibrated using laboratory drop tests. For moderately to highly fractured rock masses, the experimental results of Marchelli et al.[22] are used, while for intact brittle materials, the formulation is based on the findings of Guccione et al.[114] As discussed in Section 3.2, rotational energy is not considered in the present formulation, as the experimental data were obtained under conditions where rotational velocities before and after impact were negligible. Furthermore, it is important to note that all tests were conducted with impacts normal to the slope surface.

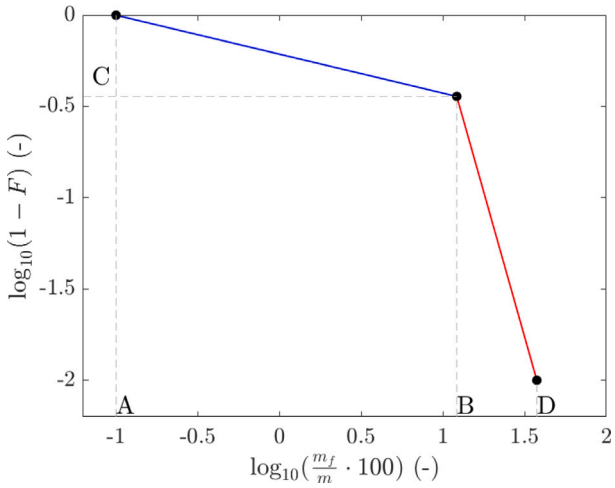


Fig. 3. Representative bilinear distribution of fragment sizes obtained from laboratory drop tests.

The absolute rebound velocity of each fragment, denoted v_f^a, is computed by considering two main mechanisms of energy dissipation during impact: (i) elasto-plastic deformation of the block and the impacted surface, and (ii) fracture formation associated with fragmentation. The total post-impact kinetic energy is then distributed among the fragments proportionally to their mass, following the approach proposed by Matas et al.[9] and Lanfranconi et al.,[19] obtaining v_f^a. The energy retained in the normal direction after impact is given by:

$$E_{k_t,n}^a = \sum_{i=1}^{n_f} \frac{1}{2} m_{f,i} (v_{f,i}^a)^2 = E_{k_t,n}^b COR_n^2 - E_{fr}, \tag{6}$$

where E_{fr} is the energy dissipated in the creation of fracture surfaces, proportional to the fracture area and the surface energy per unit area of the block. Based on the experimental campaign by Marchelli et al.[22] and Guccione et al.,[114] the combined effect of rebound and fracture energy loss can be expressed as:

$$E_{k_t,n}^a = \sum_{i=1}^{n_f} E_{k_t,n,f,i}^b COR_{*,i}^2, \tag{7}$$

where $COR_{*,i}$ is the effective restitution coefficient for the ith fragment, implicitly accounting for both rebound and fracture energy dissipations. Since fragmentation occurs at impact, the fragments do not possess pre-impact kinetic energy. Instead, the initial kinetic energy of each fragment $E_{k_t,n,f}^b$ is derived from the impacted block and distributed proportionally to its mass, ensuring conservation of energy and consistency with observed post-impact behaviour.

In the proposed model, the effective restitution coefficient COR_* varies according to the rock mass condition and the joint inclination θ relative to the impacted surface, while experimental data[22,114] indicate that COR_* is not significantly influenced by impact energy. Table 5 summarises the statistical distribution types that best fit the experimental data for each condition. For moderately fractured rock masses, the influence of joint orientation is explicitly considered, with distinct COR_* ranges assigned to three angular categories, corresponding to the classification adopted for data processing and interpretation of restitution behaviour in the experimental analyses of Marchelli et al.[22]

Since the available experimental data were obtained from vertical drop tests on a smooth concrete surface, the restitution coefficients derived from these tests are specific to that material configuration. To

Table 5
Statistical distribution types for the effective restitution coefficient COR_* under different rock mass conditions and joint inclinations θ relative to the impacted surface.

Rock mass condition	θ (°)	Probability density function of COR_*
Intact	–	Uniform(0.16, 0.31)
Moderately fractured	$0° \le \theta \le 15°$	$0.26 \cdot \text{Beta}(4,4) + 0.05$
	$15° < \theta < 75°$	Uniform(0.10, 0.29)
	$75° \le \theta \le 90°$	$0.24 \cdot \text{Beta}(3,2) + 0.15$
Highly fractured	0°–90°	Uniform(0.04, 0.46)

Table 6
Statistical distribution types for ψ under different rock mass conditions and joint inclinations θ relative to the impacted surface.

Rock mass condition	θ (°)	Probability density function of ψ
Intact	–	Uniform (0.47, 0.91)
Moderately fractured	$0° \le \theta \le 15°$	$0.76 \cdot \text{Beta}(4,4) + 0.15$
	$15° < \theta < 75°$	Uniform (0.29, 0.85)
	$75° \le \theta \le 90°$	$0.71 \cdot \text{Beta}(3.2) + 0.44$
Highly fractured	0°–90°	Uniform (0.12, 1.35)

generalise the model and apply COR_* to other geological contexts, a scaling factor ψ is introduced. This factor allows decoupling the restitution coefficient from material-specific calibration by relating the observed COR_* to the restitution coefficient of an intact sphere on the slab adopted in the experimental campaign. This normal restitution coefficient, equal to 0.34, is obtained adopting the Stronge's formula[115] for the impact of an elastic–perfectly plastic sphere impacting a planar surface at 7 m/s. Table 6 summarises the statistical distribution types that best fit the experimental data for each condition. The effective restitution coefficient for each fragment can thus expressed as:

$$COR_{*,i} = \psi\, COR_n, \tag{8}$$

where COR_n is the normal coefficient of restitution computed for the block–slope interaction. The norm of the post-impact velocity vector due to normal impact of the ith fragment, denoted $\tilde{v}^a_{f,i}$, is thus obtained as:

$$\tilde{v}^a_{f,i} = v^b_{n,B} \cdot \psi\, COR_n. \tag{9}$$

To derive the vectorial components for each fragment, the angle α between the normal and tangential components of $\tilde{v}^a_f$, i.e. $\arctan\left(\tilde{v}^a_{f,n}/\tilde{v}^a_{f,t}\right)$, is sampled from a distribution derived from experimental observations. Given $\tilde{v}^a_f$, the velocity components of each fragment are computed as:

$$v^a_{f,n} = \tilde{v}^a_f, \sin\alpha \tag{10}$$

and

$$v^a_{f,t} = \pm(\tilde{v}^a_f \cos\alpha) + v^b_t COR_t \tag{11}$$

where v^b_t is the tangential component of the block's pre-impact velocity. Although α is defined as positive, the post-impact velocity vector may have an upslope tangential direction. To reflect this, a random sign is assigned to $\tilde{v}^a_f \cos\alpha$. The second term in the tangential velocity accounts for the residual tangential energy transferred from the parent block to the fragment. The two components $v^a_{f,n}$ and $v^a_{f,t}$ thus define the post-impact velocity vector of the fragment, v^a_f.

Experimental results[22,114] indicate that the angle α varies between a minimum and maximum value depending on three key factors: the rock mass condition, the joint inclination θ relative to the impacted surface, and ϵ. These bounds, illustrated in Fig. 4, reflect the influence of structural configuration and impact conditions on fragment ejection direction. For a given impact energy within the experimentally investigated range, a value of α is sampled via Monte Carlo extraction from a uniform distribution bounded by the corresponding minimum and maximum values. In cases where the impact energy exceeds the tested domain, the extraction range is extrapolated by assuming the same minimum and maximum bounds as those observed at the highest investigated ϵ, ensuring continuity with the experimental trend. The reference bounds and extrapolation approach are illustrated in Fig. 4. A complete numerical example combining Eqs. (2)–(11) into a single calculation workflow is provided in Appendix B.

Table 7
Mean and standard deviation (Std. Dev.) of physical and mechanical parameters for block and slab materials.

Parameter	Mean	Std. Dev.
d_{eq} (m)	0.100	–
ρ (kg/m^3)	2000	–
σ_t (MPa)	2.00	0.18
Y_b (MPa)	2050	223
ν_b (–)	0.25	0.02
Y_s (MPa)	11 700	1000
ν_s (–)	0.15	0.01

4. Model calibration and validation

The proposed model underwent a preliminary validation based on targeted comparisons with laboratory experiments and real-scale data available in the literature, focusing on key components of the simulation framework. In particular, the validation addressed: (i) the fragmentation threshold module, assessing its ability to reproduce fragmentation probability under varying impact conditions; (ii) the size distribution of the fragments; (iii) the run-out distribution, evaluating the post-impact travel distances of fragments along the slope surface; (iv) shape-dependent rockfall propagation and fragmentation. For kinematic outputs (e.g. velocity, trajectory height), no predefined probability distribution can be assumed a priori.[116] The resulting distributions are typically skewed due to impact thresholds, energy dissipation and fragmentation processes. For this reason, median values are reported and compared, as they provide a more robust estimator of central tendency than the mean in non-Gaussian distributions.

4.1. Fragmentation threshold validation

The fragmentation threshold module was first validated using laboratory drop tests on mortar spheres with embedded discontinuities, as described in Marchelli et al.[22] These tests investigated the influence of impact velocity, discontinuity density, and orientation with respect to the impacted surface on fragmentation probability and post-impact behaviour. Multiple impact velocities were tested, ranging from 5 to 10 m/s, with systematic variation of the discontinuity plane orientation relative to the impacted surface. Numerical simulations replicated these conditions using the same mechanical properties for the mortar spheres[22] and the concrete slab.[114] Table 7 reports the mean values and experimentally derived standard deviations adopted also in the simulations.

To evaluate the effectiveness of the Monte Carlo sampling approach for discontinuity orientation and the application of an orientation-dependent reduction coefficient to tensile strength, fragmentation probabilities obtained through the model and those gained from the experiments were compared across different impact velocities. This approach is specifically applied to moderately fractured rock mass conditions. For the validation, the experimental configurations with a single discontinuity reported in Marchelli et al.[22] were chosen to represent intermediate structural weakening, i.e. moderately fractured condition. In detail, the 1–2Ds series have a discontinuity located at the centre of the sphere, while the 1–4Ds series have a discontinuity positioned at one-quarter of the diameter. Table 8 presents the results for both experimental and numerical cases.

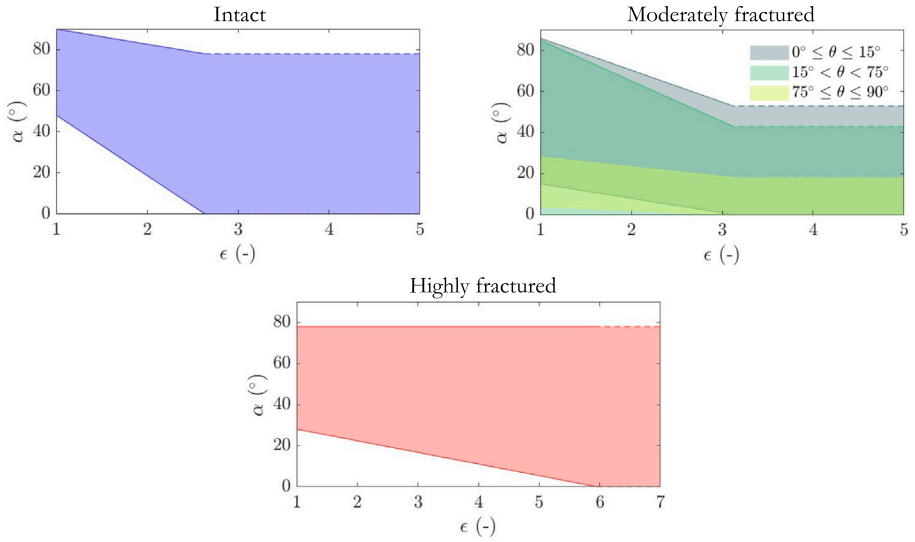


Fig. 4. Angular range of fragment ejection direction (α) as a function of rock mass condition, joint inclination θ, and impact energy ratio $\epsilon = E^b_{k_i,n}/E_{th}$. Solid lines represent the range investigated in laboratory experiments, while dashed lines indicate extrapolated bounds beyond the tested domain.

Table 8
Comparison of experimental (exp., from Marchelli et al.[22]) and numerical (num.) fragmentation results, including impact velocity and drop height. Mod. fract. refer to moderately fractured rock mass conditions. Note that at 8.5 m/s, only the 1–2Ds configuration was tested experimentally.

Configuration	Impact velocity (m/s) (Drop height (m))	No. of tests/simulations (–)	% fragmented
1–2Ds (exp.)	6.0 (1.865)	53	53
1–4Ds (exp.)		24	58
Mod. fract. (num)		1000	57
1–2Ds (exp.)	7.0 (2.497)	52	85
1–4Ds (exp.)		25	76
Mod. fract. (num.)		1000	90
1–2Ds (exp.)	8.5 (3.682)	15	100
Mod. fract. (num.)		1000	100
1–2Ds (Exp.)	10.0 (5.097)	20	100
1–4Ds (Exp)		21	100
Mod. fract. (num.)		1000	100

The comparison between experimental and numerical fragmentation rates shows a very good agreement across all tested velocities for moderately fractured rock mass conditions. The numerical model reproduces the observed trends with high consistency, confirming its validity. The percentage error remains below 5% at 6 m/s, and below 10% at 7 m/s. At 8.5 and 10 m/s, both experimental and numerical results converge to 100% fragmentation, indicating full breakage under high-energy impacts. It should be noted that in the laboratory tests, the discontinuity pattern is fixed and precisely controlled, allowing for systematic variation of orientation and position. In contrast, the numerical model generalises the variability of natural rock masses by encompassing spacing, orientation, and density of discontinuities into a single probabilistic category. These results support the robustness of the energy-based threshold formulation and the probabilistic treatment of discontinuity orientation.

A qualitative comparison was also carried out with the field-scale impact tests on Beola orthogneiss blocks reported by Giacomini et al.[66] Characterised by persistent planes of weakness but exhibiting less schistosity than the other investigated lithology (Serizzo), the mechanical behaviour of Beola can, in a qualitative sense, be regarded as broadly comparable to the moderately fractured class considered in the present work. This approximation is used only to provide a broad consistency check, not for calibration. For each Beola test (B1–B10), the impact energy E^b_k was taken directly from the in situ measurements reported by Giacomini et al.,[66] while the fragmentation threshold E_{th} was estimated using Eq. (2) through conversion of the initial volumes into equivalent diameters and the incorporation of the measured angle between the foliation and the impacted surface (corresponding to the inclination θ in the present formulation).

Test B1 is noteworthy in that the block broke into two pieces, suggesting that the impact energy was close to the threshold. The inclination θ of approximately 10° implies that the effective tensile resistance is essentially that of the intact matrix ($k_o \approx 1$), yielding $E^b_k \approx E_{\text{th}}$. Using B1 as a reference, the ratio E^b_k/E_{th} was evaluated for the remaining Beola tests. From B1 to B10, all cases exhibit $E^b_k/E_{\text{th}} > 1$, consistent with the fact that every Beola block in the in situ campaign fragmented under impact. Table 9 summarises the impact energies from Giacomini et al.,[66] together with the initial volumes used to derive the equivalent diameters d_{eq} for estimating E_{th} via Eq. (2). Since the present comparison is qualitative, the threshold values are placeholders until material parameters for Beola are provided; however, the tabulated structure illustrates how the proposed threshold framework can be applied to field-scale data for consistency checks.

Tests B2 and B3, which have similar θ and comparable volumes, present closely aligned fragmentation outcomes, in agreement with the model. Moreover, for comparable impact energies, increasing the inclination of the foliation relative to the impacted surface leads to more intense fragmentation, a trend consistent with the behaviour predicted by the proposed model for moderately fractured rock masses. Although Giacomini et al.[66] concluded that a single universal impacting-energy threshold for fragmentation could not be identified, the experimental trends nonetheless suggest that an energy threshold dependent on rock–mass condition and orientation of the discontinuities with respect to the impacted surface is reasonable. Although qualitative, this agreement supports the physical plausibility of the adopted formulation.

Furthermore, when considering tests with similar inclination but distinctly different volumes, the observations indicate that a classical size-effect law based solely on a monotonic reduction of tensile strength with increasing volume is not suitable for describing the fragmentation behaviour of anisotropic rock. In the Beola dataset, differences in fragmentation intensity are governed far more by microstructural anisotropy, foliation orientation, and impact configuration than by any simple tensile-strength scaling. Hence, a reduction of $\bar{\sigma}_t$ with size, as prescribed in certain fracture-mechanics-based size-effect laws, does not reflect the mechanisms observed in the field and,

Table 9
Beola field tests from Giacomini et al.[66]: impact energy E_k^b, inclination θ, number of fragments (n_f), and qualitative comparison with the estimated fragmentation threshold E_{th}.

Test	Initial volume V_0 (m^3)	θ (°)	E_k^b (kJ)	n_f (–)	E_{th} (kJ)	E_k^b/E_{th}
B1	0.45	10	116	22	116.00	1.00
B2	0.64	75	165	0	102.14	1.62
B3	0.70	80	181	22	111.72	1.62
B4	1.01	80	261	9	161.19	1.62
B5	1.02	70	263	13	162.79	1.62
B6	0.38	60	198	4	60.65	3.26
B7	1.14	55	588	5	181.94	3.23
B8	0.86	75	444	14	137.25	3.23
B9	0.45	15	352	8	116.00	3.03
B10	0.43	30	442	15	110.84	3.99

albeit qualitatively, further strengthens the rationale of the proposed formulation.

In practice, fully documented natural rockfall cases suitable for validating fragmentation-aware trajectory models are rare, as most events are only partially characterised in terms of impact sequence, kinematics and fragmentation details. A complementary consistency check based on a documented natural rockfall case[11] is therefore provided in Appendix C, to illustrate the applicability and current limitations of the fragmentation threshold formulation when field data are only partially constrained.

4.2. Fragments size distribution validation

The validation of the fragment size distribution was performed by comparing the empirical cumulative distribution functions obtained from experimental drop tests and numerical simulations. Experimental data refer to the 1–2Ds and 1–4Ds configurations, tested at three impact velocities (v_i = 6, 7, and 10 m/s), while numerical simulations were carried out under equivalent conditions. In all cases, a threshold of 5% of the initial block mass was applied to exclude excessively small fragments.

Fig. 5 illustrates the comparison between the empirical cumulative fragment size distributions obtained from experimental drop tests (1–2Ds and 1–4Ds configurations) and numerical simulations for three impact velocities. The numerical distribution corresponds to the median cumulative response obtained from an ensemble of N_{sim} = 1000 Monte Carlo realisations.

At low impact velocities (v_i = 6 m/s), some differences between experimental and numerical curves are noticeable. At this velocity, which corresponds to a kinetic energy close to the fragmentation threshold for an intact sphere as proposed herein, fractures typically propagate along the discontinuity plane. Recalling what reported in Marchelli et al.,[22] in the 1–2Ds configuration, this often results in two large fragments corresponding to the two halves of the sphere, while in 1–4Ds, the fracture typically separates the block into portions of approximately 20% and 80% of the initial mass. These structural constraints produce distinct steps in the cumulative curves. Conversely, the numerical model does not impose fixed discontinuity positions. Instead, it applies a probabilistic approach to represent variability in joint orientation and spacing, leading to smoother distributions and a more gradual increase in cumulative probability.

At intermediate velocity (v_i = 7 m/s), the agreement improves as fractures begin to propagate beyond the discontinuity planes, reducing the influence of fixed joint positions. The percentage error in median fragment size between numerical and experimental cases is approximately 12% for 1–2Ds and 9% for 1–4Ds.

At high velocity (v_i = 10 m/s), where breakage in the experiments involves both discontinuities and intact material, the curves align closely. The maximum deviation in cumulative probability at 50% mass is less than 5%, confirming that the model accurately reproduces fragmentation behaviour when structural control becomes secondary to impact energy. These results support the validity of the probabilistic approach for fragment size distribution under dynamic loading conditions. For this case, the energy ratio reaches $\epsilon \approx 3.12$, well above the fragmentation threshold, and in general applications, scenarios with even higher ϵ values can occur, further confirming the robustness of the model under extreme impact conditions.

Table 10
Mechanical properties and model parameters used for the Vallirana quarry simulations. Mechanical parameters measured by Ruiz-Carulla et al.[117] were used for both slope and block. Model interaction parameters were derived by back-analysis.

Category	Property	Value	Assumed Std. Dev.
Mechanical	σ_t (MPa)	4.1 (from Brazilian tests)	0.4
Mechanical	$Y_B = Y_s$ (GPa)	119 (from uniaxial compressive tests)	12
Mechanical	ρ (kN/m^3)	26.5	1.0
Mechanical	$\nu_B = \nu_s$ (–)	0.2[a]	0.02
Model	COR_{n0}	0.4[a]	0.04
Model	COR_t	0.6[a]	0.04
Model	ϕ (°)	30[a]	3
Model	N_{sim} (–)	1000	–

[a] Values marked assumed for numerical analysis.

4.3. Fragments travel distances validation

To assess the reliability of the proposed model in simulating fragment travel distances, available field data from large-scale rockfall experiments were used. Specifically, the tests conducted by Gili et al.,[13,112] Ruiz-Carulla et al.[117] and Matas et al.[9] in the Foj limestone quarry in Vallirana (Barcelona, Spain) provide the most comprehensive dataset currently available. This site was selected due to the homogeneity of the lithology, i.e. massive limestone, for both the slope and the released blocks, and the availability of detailed mechanical characterisation, as reported in Table 10.

The experimental campaign included four test sites, of which sites 1, 2, and 4 (as named in the referenced papers) were located in the Vallirana quarry. These sites were selected within a steep slope bench where the rock was barely fractured, ensuring sufficient stiffness to promote block breakage. Blocks were transported and released using a construction dozer; the blocks were allowed to fall freely from the blade. Site 1 corresponds to a single steep bench, where 30 blocks were released above the crest at an average height of 17.45 m from the quarry bottom. The slope profile consisted of a high-angle plane with no major discontinuities, designed to favour tangential impacts. All blocks experienced two impacts before reaching the quarry bottom, with the first occurring on the inclined slope and the second on the nearly horizontal platform at the base. In site 4, the slope consisted of a 42.4° inclined plane, coinciding with a natural discontinuity surface, followed by a nearly horizontal platform with a thin soil layer over bedrock. The elevation difference between the crown and the foot of the slope is approximately 19 m. This configuration is particularly favourable to fragmentation, and site 4, from which 24 blocks were released, yielded the highest number of fragments among all tests, with only two blocks remaining intact.

The mechanical parameters measured by Ruiz-Carulla et al.[117] were adopted in the numerical model for both the slope and the blocks. Standard deviations were assumed equal to 10% of the corresponding measured mean values, as only mean material properties were available. This assumed variability is consistent with that observed in controlled laboratory experiments on brittle materials, as discussed in Section 4.1. All numerical simulations were performed assuming intact rock properties consistent with the limestone description by

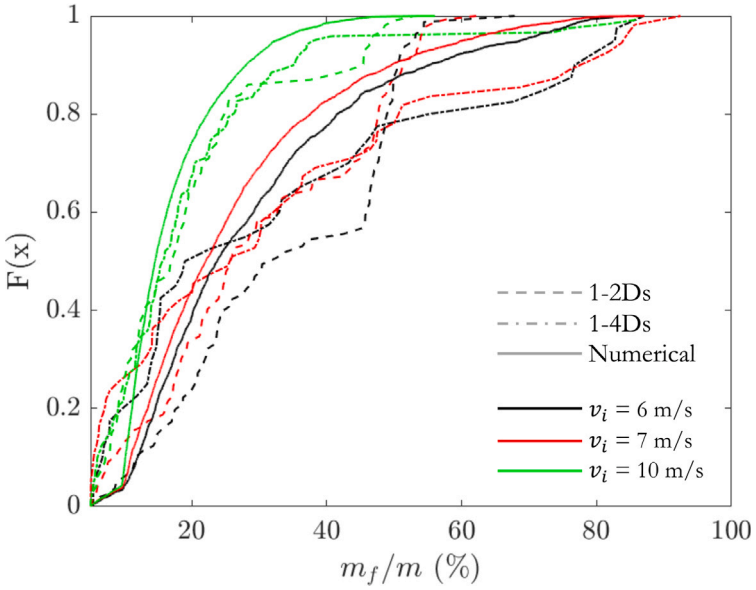


Fig. 5. Empirical cumulative fragment size distributions for experimental (1–2Ds and 1–4Ds) and numerical cases at three impact velocities. The numerical curve represents the median cumulative distribution obtained from the ensemble of Monte Carlo simulations. In all cases, the threshold for fragment size was set at 5% of the initial mass.

Ruiz-Carulla et al.,[117] reflecting the homogeneous lithology of the Vallirana quarry. To avoid introducing additional variables related to block geometry, and given the absence of precise information on the shape of the released blocks, spherical samples were assumed, and the median block volume of approx. 1.13 m^3, i.e. d_{eq} = 1.29 m was used to represent typical conditions at each site. The calibration of the rebound parameters was performed using data from site 1, where blocks remained intact after impact. Specifically, COR_{n0} and COR_t were adjusted to match the observed impact velocity and angle at the second impact, as reported in Supplementary Material 7 of Gili et al.[13] These data, which include initial block volume and kinematic conditions at both impacts, enabled site-specific calibration of rebound behaviour in the absence of fragmentation. The interaction parameter ϕ was instead assumed equal to 30°. A total of N_{sim} = 1000 blocks were released, with an initial horizontal velocity of 0.2 m/s, according with the recommendation by Matas et al.[9] to reproduce the crane-induced motion during block release. Unless otherwise stated, the number of simulations adopted in this study guarantees convergence of the reported probabilistic indicators within 1%. The consistency and convergence of the fragmentation simulations with respect to the number of Monte Carlo realisations are analysed in Appendix D. The back-analysed simulation parameter are reported in Table 10. Fig. 6 illustrates the simulated trajectories for Site 1, while Table 11 summarises the observed and numerical values for block volume V_b, impact velocity $v_{i,2}$, and impact angle $\iota_{i,2}$ at the second impact[13]

An assessment of the suitability of the calibrated parameters was then carried out using site 4, where the runout distance of intact blocks is known to be approximately 35 m (Table 11). However, only two blocks remained intact after impact, limiting the available data for rebound assessment.

The comparison between observed and simulated runout distances at Site 4 demonstrates a strong agreement, with the numerical median value (31.2 m) falling within the observed range and showing a percentage error of 8%. It should be noted that, according to Matas et al.,[9] the released blocks originated from an elevation approximately 8–10 m above the first impacted point; however, no further detail is provided regarding the 24 tests. As a result, a mean value was assumed in the simulation, which may contribute to discrepancies in the computed impact angle $\iota_{i,2}$.

Subsequently, a first attempt to validate the fragmentation module was carried out at site 4, which experienced the highest fragmentation rate: only two of the 24 released blocks remained intact after impact, resulting in 1241 measured fragments. A cumulative plot of fragment number versus runout and a cumulative plot of fragment volume versus runout are available in Matas et al.,[9] providing a basis for comparison with the fragmentation module proposed herein. Although this does not constitute a formal validation, it represents the closest available benchmark for assessing model performance under real-scale fragmentation conditions. For these numerical analysis, a block volume of 1 m^3 was assumed for the fragmentation module. This value is consistent with the median volume (0.87 m^3) and close to the mean volume (1.06 m^3) calculated across all test sites. From Figures 8 and 9 of Matas et al.,[9] the minimum, median, and maximum runout distances, together with the runout distance corresponding to the position where half of the total thrown mass had stopped, were derived and are reported in Table 12, allowing a direct comparison with the numerical results. Fig. 7 provides an example of the fragmentation module in action, showing only one block release. The plotted trajectories correspond to the fragments generated during impact.

The comparison in Table 12 indicates that the numerical model reproduces the observed runout behaviour with good accuracy. The minimum and maximum runout distances differ by less than 20% and 5%, respectively, suggesting that the model captures the overall dispersion range effectively. The runout corresponding to 50% cumulative

Table 11
Comparison of observed and numerical values for block volume V_b, impact velocity $v_{i,2}$, and impact angle $\iota_{i,2}$ at second impact. Values marked with * are assumed for numerical analysis[13]. For site 4, only two blocks remained intact at the second impact. In this case, the runout distance (X_{end}) is derived from[9]. The percentage error refers to the difference between observed and numerical median values.

Site	Quantity	Observed median (Min–Max) values	Numerical median (Min–Max) values	% error
Site 1	V_b (m^3)	1.13 (0.19–4.59)	1.13	
Site 1	$v_{i,2}$ (m/s)	14.3 (12.7–15.9)	14.9 (11.0–15.7)	4.2%
Site 1	$\iota_{i,2}$ (°)	59 (48–85)	66.4 (62-68)	12.5%
Site 4	V_b (m^3)	0.61 (0.50–0.71)	0.61	
Site 4	$v_{i,2}$ (m/s)	16.4 (15.9–16.8)	17.0 (16.1-18.2)	3.9%
Site 4	$\iota_{i,2}$ (°)	81 (80–82)	70 (65–72)	13.6%
Site 4	X_{end} (m)	≈35	32.2 (25.9–35.7)	8.0%

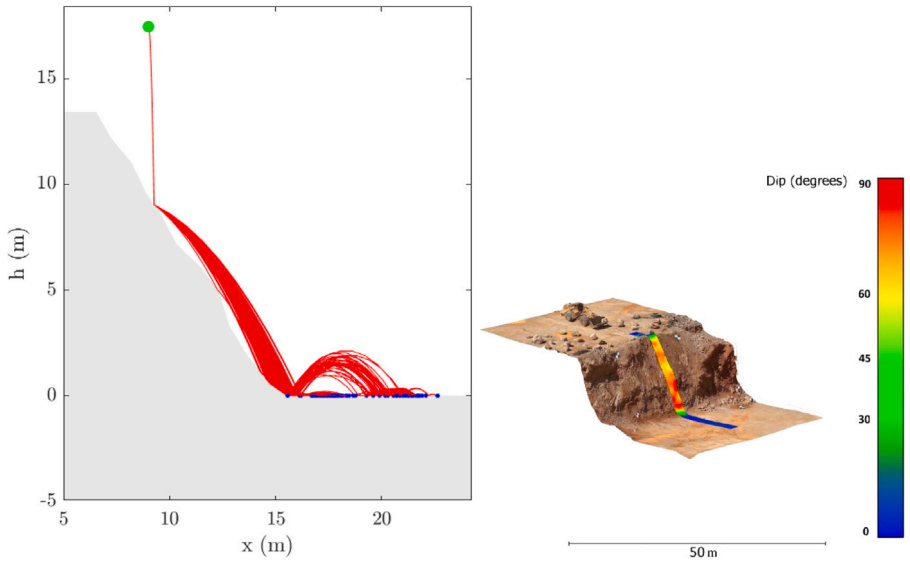


Fig. 6. Simulated trajectories for Site 1. The release point is shown in green, trajectories in red, and end points in blue. The grey area represents the slope profile. The right sketch illustrates a 3D view of the slope, from Gili et al.[13]

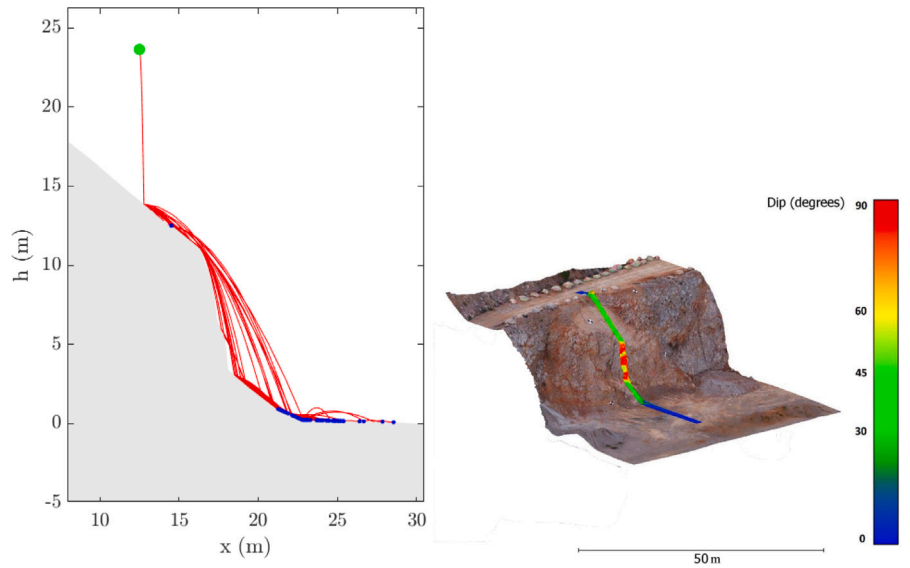


Fig. 7. Simulated trajectories for Site 4. Only one block release is shown, and the plotted trajectories correspond to the fragments generated during impact. The release point is shown in green, fragment trajectories in red, and end points in blue. The grey area represents the slope profile. The right sketch illustrates a 3D view of the slope, from Gili et al.[13]

Table 12
Comparison of observed[9] and numerical runout distances (X_{end}) of fragments, including percentage error.

Statistic	Observed (m)	Numerical (m)	% error
Minimum runout	12.0	14.3	19.2%
Median runout	≈17	22.8	33.9%
Runout at 50% cumulative mass	≈13.5	14.6	8.1%
Maximum runout	35.2	33.65	4.4%

mass is almost identical between observed and simulated cases, confirming that the model provides a realistic representation of fragment distribution along the slope. The median runout is slightly overestimated, which may reflect the influence of idealised slope geometry, the assumption of spherical blocks in the simulation (given that block shape in the field tests was unknown and variable) and uncertainties related to the precise topography and release position in the field tests. This slight overestimation may also partly reflect the two-dimensional formulation of the model, which constrains fragmentation energy within the longitudinal profile and does not account for out-of-plane energy dissipation through lateral dispersion.

While further experimental data would strengthen this assessment, the calibration and comparison with Vallirana field data already offer a practical indication of the model's capability to reproduce fragment travel distances for both intact and fragmented blocks.

4.4. Shape-dependent rockfall propagation and fragmentation validation

A complementary validation of the propagation model was performed using the full-scale rockfall experiments conducted by Bourrier et al.[118] in the Authume quarry (France). The site is underlain by pink Callovian limestone, with terrain strongly modified by quarrying and characterised by vertical cuts, berms and gently inclined waste deposits. Two distinct propagation paths were tested (path A and path B),

Table 13
Summary of experimental inputs and outputs for the Authume quarry tests. Data from[40] (shape distribution in deposits; C = compact, E = elongated). The key for deposit zones is reported in Fig. 8.c.

Parameter	Path A	Path B
N° of released blocks	41	47
Release height (m)	4	2
Mass range (kg) (50th percentile in brackets)	178–1751 (679)	170–1869 (684)
N° and % of fragmented blocks	11 (27%)	1 (2.1%)
% of deposited blocks in zone (%)	1A: 2.4 2A: 2.4 3A: 48.8 4A: 46.4	1B: 8.5 2B: 6.4 3B: 68.1 4B: 17.0
Shape distribution in deposit zone (%)	1A: 0 C; 2.4 E 2A: 0 C; 2.4 E 3A: 22.0 C; 26.8 E 4A: 34.2 C; 12.2 E	1B: 0 C; 8.5 E 2B: 0 C; 6.4 E 3B: 31.9 C; 34.0 E 4B: 17.0 C; 2.2 E

chosen specifically because they represent challenging configurations for trajectory models (Fig. 8). Path A consists of an upper gentle slope (32°) composed of dry quarry waste (sand–clay mixture with limestone fragments), followed by a flatter and rougher transition zone, and then by two subvertical limestone cuts separated by a horizontal track. The toe area is a quasi-horizontal platform of compact soil. Path B begins with a 40 m-long slope inclined at 32°, bounded mid-way by a rock cut on one side and a talus on the other forming a corridor. Below, two successive tracks and an additional slope lead to the final deposit area. The upper section of path B is vegetated, while the corridor and the intermediate slopes consist of medium-soft quarry waste. Fig. 8 reports the deposit areas of the blocks (Fig. 8.b), the 2D profiles along the main rockfall paths (Fig. 8.c,d), and the maps of block stopping points classified according to block mass (Fig. 8.e) and block shape (Fig. 8.f).

In the experimental programme, 41 blocks were released on path A and 47 on path B. Blocks were dropped from a height of 4 m on path A and 2 m on path B. The volumes ranged between 0.1 m^3 and 0.75 m^3. Fragmentation occurred mainly on path A, where 27% of blocks broke, typically after a normal impact on flatter zones, whereas only one block fragmented on path B. Runout distances exhibited clear preferential deposit zones: on path A, 48.8% of blocks stopped on the intermediate track and 46.2% reached the lower platform; on path B, 68.1% stopped on the second track and 17% reached the terminal platform (Table 13). The observed behaviour also revealed a strong influence of block characteristics: compact blocks tended to travel further, while elongated blocks were more often arrested in the upper parts of the paths.[40,118] To provide a structured summary for model comparison, Table 13 reports key input data and outputs for the two paths, extracted from.[40,118]

Because no mechanical characterisation of the pink Callovian limestone was performed in the tests, high-quality limestone parameters are assumed for the simulations: Young's modulus $Y_B = 30$ GPa and tensile strength $\sigma_t = 7$ MPa, consistent with representative values for strong limestones.[119] To encompass epistemic uncertainty associated with these assumed properties, a coefficient of variation equal to 10% of each parameter value was adopted in the simulations. All numerical simulations were performed assuming intact rock properties consistent with this rock type.

The validation proceeded in three consecutive steps. First, restitution parameters were calibrated using path B, which is almost entirely fragmentation-free and therefore provides consistent kinematic data for tuning the normal and tangential restitution coefficients so that simulated runout distances, velocities and passage probabilities match the observations of Bourrier et al.[118] Once these parameters and the soil-dissipation properties were established, they were applied to the simulation of path A, where fragmentation occurs more frequently.

Table 14
Model parameters used for path B. The listed values represent the mean of the calibrated distributions, while values in parentheses indicate the corresponding standard deviations. Standard deviations are assumed equal to approximately 10% of the corresponding mean values, a range commonly adopted in probabilistic rockfall modelling to encompass uncertainties.[88,120] For restitution coefficients, values are constrained to physically admissible limits (maximum equal to one).

Slope surface material	COR_{n0} (–)	COR_t (–)	ϕ (°)
Sane rock	0.55 (0.05)	0.90 (0.05)	8 (1)
Altered rock	0.50 (0.05)	0.90 (0.05)	8 (1)
Quarry waste	0.40 (0.04)	0.85 (0.04)	8 (1)

Despite the fact that most experimentally tested blocks fall into the compact or compact-bladed categories (as also simulated by Garcia et al.[40]), the influence of block morphology was further examined by performing simulations with all the available shape classes. This extended analysis enables the assessment of the sensitivity of propagation distances and deposition patterns to variations in block shape and provides a robust test of the model's capacity to reproduce the observed variability in block kinematics.

For the calibration stage, Table 14 lists the parameters that provide the best fit between the experimental cumulative distribution of runout distances and the numerical results for path B (Fig. 9). A total of 1000 simulations was found to be sufficient to ensure statistical stability of the results, and a variability of 20% around the median value of the initial mass was assumed to reflect the variability in the block size adopted in the experiments. Overall, the agreement between the experimental and numerical ECDFs for path B is very good, confirming that the calibrated parameters successfully encompass the assumptions of the lumped-mass model, accounting for the rolling behaviour observed in the field. A discrepancy is nevertheless visible in the intermediate runout range (approximately 40–55 m), where the numerical curve shows a locally steeper increase. This deviation can be linked to the shallow topographic depression along path B (Fig. 9), which in the simulations favours the early arrest of blocks and results in a local accumulation of stopping points. In the field, several blocks rolled across this concave section with small but non-negligible rotational velocity and near-zero passing height, allowing them to regain momentum and travel beyond the depression. In this context, the exact location and extent of the release zone are only approximately known from the available references, introducing aleatory uncertainty in the initial kinematics that may shift part of the deposition in this segment. Moreover, although the analysis is conducted along the preferential 2D propagation path, minor three-dimensional effects in the real tests, such as slight lateral deviations within the corridor, cannot be reproduced in a strictly 2D framework. Importantly, these small-scale deviations do not affect the overall match between experimental and numerical runout distributions. A comparison at the evaluation screens can be made in terms of passing height rather than translational velocity, since the latter in the model incorporates both translational and (implicitly) rotational contributions, whereas the experimental dataset separately reports the proportion of blocks rolling in contact with the slope. The exact location of the collectors is not reported in the references; therefore, for the numerical results, the 95% percentile range of trajectory heights was extracted within a 5 m window around the approximate collector positions. Table 15 summarises the comparison for c–B1 and c–B2. The comparison confirms that the numerical trajectories reproduce the observed trend: passing heights remain very small at both collectors, consistent with rolling or near-rolling motion on the waste-material stretches of path B.

For path A, the experimental dataset shows a clear predominance of equant blocks, whereas flat, blade and rod-like shapes represent smaller fractions (Table 16). Fragmentation occurred most frequently among rod-shaped blocks, followed by equant blocks and flat blocks, while the single blade-shaped block did not fragment. As reported by

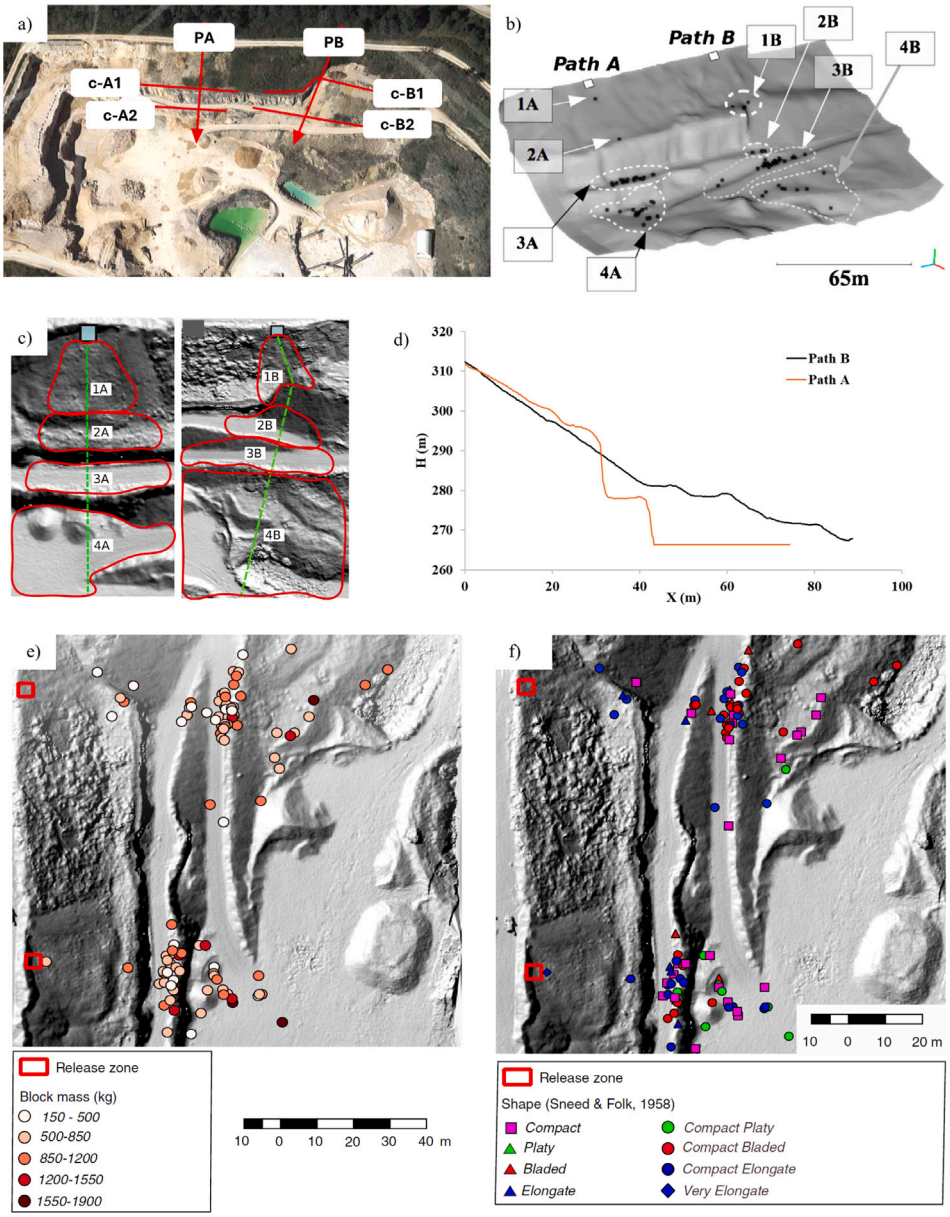


Fig. 8. (a) Aerial view of the Authume quarry showing the two propagation profiles, path A (PA) and path B (PB), together with the virtual barriers c–A1, c–A2, c–B1, and c–B2 (from, Garcia et al.[40] adapted); (b) final positions of the blocks represented as black points, with preferential deposit zones shown on the right and denoted "A" for path A and "B" for path B (from Bourrier et al.[118]); (c) planimetric view of the preferential deposit zones identified during the experimental campaign, with indication of the 2D profiles along the main rockfall paths (from Bourrier and Acary[38]); (d) 2D profiles; (e) map of block stopping points classified according to block mass (from Bourrier et al.[118]); (f) map of block stopping points classified according to block shape categories (from Bourrier et al.[118])

Table 15
Comparison between numerical and experimental passing heights at collectors c–B1 and c–B2.

Collector	Numerical (95th-percentile)	Experimental passing heights
c–B1	0.4–3.0 m	84% in contact with the slope; 14% between 0.5–1 m; 2% between 1–3 m
c–B2	1.0–1.4 m	70% in contact with the slope; 30% between 0.5–1 m

Bourrier et al.,[118] fragmentation on path A typically resulted from near-normal impacts on the horizontal track or the downhill platform, often producing a complete disaggregation into small pieces. Large surviving fragments were rare; when present, their residual runout was limited (typically <1 m). Specifically, four blocks had main fragments travelling no more than roughly 1 m after breakage, and only one block produced a small secondary fragment detaching after c–A1 while the main fragment continued past c–A2 (refer to Fig. 8.a). These observations underline the strong influence of impact configuration and block geometry on runout along this path.

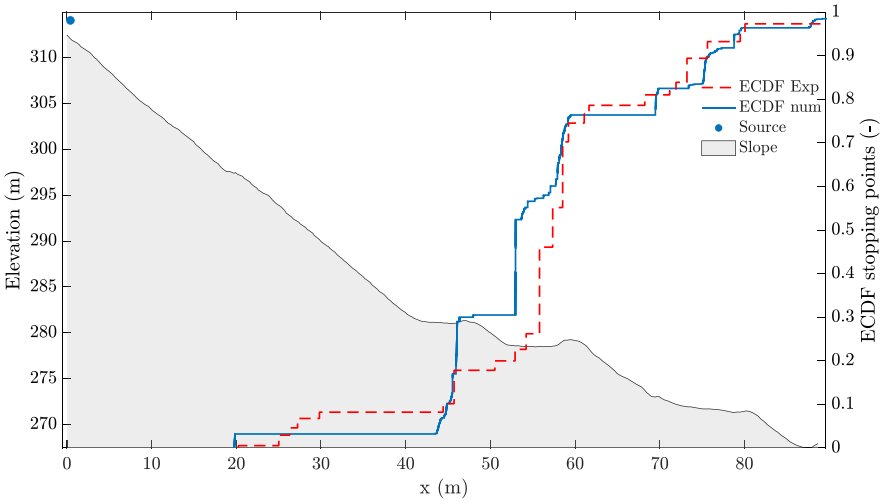


Fig. 9. Cumulative distribution functions of block propagation distances for path B, comparing the experimental campaign with the numerical results.

Table 16
Shape distribution and fragmentation outcomes for the experimental blocks released along path A.

Shape class	Released	Fragmented	Fragmented (% of class)
Flat (slab)	6	1	16.7%
Blade	1	0	0%
Equant	28	8	28.6%
Rod (elongated)	6	4	66.7%
Total	**41**	**13**	**31.7%**

Additional insight comes from the shape distribution within the deposit zones (Table 13), where compact (cubic/equant) blocks tend to reach larger distances than elongated ones, consistently with the spatial patterns visible in Fig. 8.f. This experimental evidence provides a useful benchmark for assessing the model performance under different shape assignments.

Fig. 10 compares the experimental ECDF of runout distances with numerical simulations carried out for the four representative block shapes implemented in RockFRAG (sphere, cube, slab and prism). All simulated curves capture the overall runout structure governed by the two subvertical cuts and the intermediate flat track. Clear shape-dependent effects nonetheless emerge. Slab- and prism-shaped blocks (corresponding to the flat and rod-like classes of the experimental campaign) exhibit the shortest runouts, with trajectories terminating on or immediately below the upper track (20–30 m). This behaviour reflects their strong tendency to arrest after normal impacts and matches the limited bouncing capacity observed in the field for elongated or flattened blocks. In contrast, the cube and sphere shapes produce substantially longer runouts. The cube, which closely resembles the equant shape of most experimental blocks, provides the closest match to the experimental ECDF, whereas the sphere (not present among the released blocks) slightly overestimates the upper tail.

These differences mirror the experimental shape distribution: with more than two-thirds of the released blocks being equant, the longer runouts reproduced by the cube and sphere shapes are consistent with the dominant field behaviour. Conversely, the limited number of slab-like blocks explains why the slab-shaped numerical curve lies systematically below the experimental ECDF. Taken together, the shape-controlled simulations provide a physically consistent lower and upper bound for the expected runout behaviour on path A. The cube shape achieves the best agreement with the experimental curve, reflecting both the predominance of equant blocks in the tested population and the characteristic bouncing-dominated trajectories observed along this path.

To further explore the sensitivity of the model to both block morphology and rock–mass condition, a complementary series of simulations was performed in which the four shape classes (cube, sphere, slab and prism) were combined with the three structural categories (intact, moderately fractured and highly fractured). All simulations were initiated from the same release zone and were subjected to identical slope geometry and initial kinematic conditions, ensuring that the observed differences arise solely from shape- and structure-dependent mechanisms. The outcomes are summarised in Fig. 11, which reports: (i) the empirical cumulative distribution functions (ECDFs) of stopping points, (ii) the ECDFs of the masses of the fragments or surviving blocks, and the spatial evolution of the 95th percentile of (iii) trajectory height, (iv) velocity, (v) mass and (vi) kinetic energy along the propagation path.

Despite identical release conditions, the results display a clear divergence in behaviour between shapes and structural classes (Sp = sphere, C = cube, Sl = slab, P = prism; I = intact, MF = moderately fractured, HF = highly fractured). The mobility ranking observed in the ECDF of stopping positions does not follow a purely monotonic ordering by rock–mass condition. In particular, the stopping order for the most mobile configurations is inverted relative to expectations based on structure alone (e.g., Sp–C, Sp–MF, C–I, C–MF): spheres remain the most mobile overall, with cubes following, irrespective of whether the rock mass is intact or moderately fractured. This pattern underscores that shape exerts a predominant control on mobility, while rock–mass condition modulates (rather than dictates) the final runout envelope.

However, this shape dominance in runout is not directly transferrable to the interpretation of the fragmentation threshold. First, the ECDF of stopping points for Sp–MF shows an earlier rise than for C–I in the mid-slope range, indicating that a larger fraction of sphere–MF trajectories stop before the corresponding fraction of C-I trajectories. Second, the ECDFs of masses intersect across several configurations, signalling that the relative sequencing of mass loss is not strictly ordered by either shape or structure. These two observations caution against inferring a single, universal threshold hierarchy from runout alone. It is also important to recall that the 95th-percentile profiles

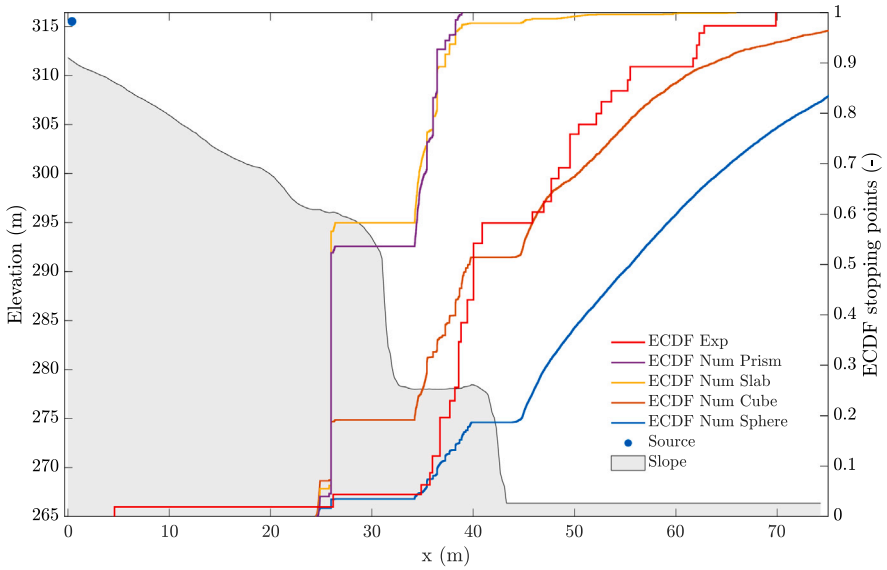


Fig. 10. Cumulative distribution functions of block propagation distances for path A, comparing the experimental campaign with the numerical results.

of height, velocity, mass and energy represent conditional statistics computed over the subset of trajectories that pass each abscissa. They do not, by themselves, convey how many blocks actually reach that position; for that, one must refer to the ECDF of stopping positions. The trends in 95th height and velocity are broadly consistent across all configurations, with peaks co-located at the two subvertical cuts. A notable exception emerges in the 95th-mass profiles for C–MF: the series displays a pronounced drop in the vicinity of the first topographic saddle, suggesting that a subset of cube–MF trajectories fragment and come to rest immediately after that impact, whereas only the residual intact (or minimally damaged) trajectories continue downslope and populate the downstream percentiles.

Taken together, these results refine the earlier reading, i.e. shape is the primary determinant of mobility, at least on path A, whereas rock–mass condition chiefly tunes the likelihood and severity of mass loss at specific impact locations. The intersections of the mass ECDFs and the local inversions in the stopping ECDF confirm that fragmentation propensity and runout do not admit a single, global ordering by structure; instead, they reflect a location-dependent interplay between impact configuration, shape-driven contact mechanics and structural weakening.

5. Conclusions and future perspectives

This study presents RockFRAG, a new probabilistic lumped-mass trajectory model that explicitly incorporates fragmentation processes in rockfall simulations. The fragmentation module accounts for the influence of impact energy, block geometry and structural features, using simplified but physically informed representations of discontinuity orientation, rock–mass quality and block shape to describe their effect on fragmentation likelihood and outcomes. Three distinct rock–mass conditions are considered: intact, moderately fractured and highly fractured, together with four representative shapes: sphere, cube, prism and slab-like. By integrating these factors, the model captures the variability of fragmentation outcomes and post-impact kinematics in a physically consistent manner. A key strength of the proposed approach lies in its probabilistic formulation. Starting from the probabilistic treatment of the threshold for fragmentation, the model includes the stochastic generation of fragment sizes and trajectories. In particular, the model combines an energy-based fragmentation threshold, influenced by material properties and structural conditions and corrected for block geometry and the relative orientation of discontinuities, with a fragment-size distribution derived from controlled laboratory tests. Post-impact kinematics are assigned using experimentally informed velocity vectors, providing a representation of rebound behaviour that remains consistent with physical observations.

The validation strategy followed a stepwise approach. First, the fragmentation threshold is shown to reproduce the observed dependence of breakage on impact energy and joint orientation, demonstrating that the model captures the transition from partial to full fragmentation as energy increases. Fragment-size distributions match the median trends and cumulative probability structure of laboratory tests for intact, moderately fractured and highly fractured conditions. Field-scale validation using the Vallirana[112] tests confirmed the ability of the model to simulate fragment travel distances and runout envelopes for intact and fragmenting blocks, despite the inherent natural variability. The Authume full-scale experiments[118] provide an assessment of model behaviour under complex topography and shape variability: shape-controlled simulations captured the divergence in runout associated with equant, elongated and slab-like geometries. The complementary sensitivity analysis further illustrates how shape and rock–mass condition jointly influence impact configuration, energy dissipation, mass loss and runout, providing a clear quantitative basis for interpreting the combined effects of geometry and structural quality. Nevertheless, while the adopted datasets provide a robust and reproducible basis for model formulation and initial validation, further calibration and validation across different lithologies, rock–mass conditions and higher impact-energy regimes (i.e. extended ranges of the energy ratio ϵ) are required to fully generalise the proposed approach. Future developments will focus on expanding the experimental database, including tests at higher impact velocities and, where feasible, additional real-scale experiments.

Although the proposed approach shows encouraging performance and captures the dominant mechanisms governing fragmentation and rockfall propagation under dynamic loading within a flexible and extensible probabilistic framework suitable for hazard assessment, several aspects remain simplified. The current two-dimensional lumped-mass formulation does not explicitly resolve lateral dispersion and the rotational dynamics effects are instead implicitly absorbed in the calibrated restitution parameters. Fragment properties after secondary breakage are, by default, inherited from the parent block, reflecting the scarcity of experimental data on post-fracture anisotropy. Similarly, the treatment of discontinuities is probabilistic rather than explicit, such that the structural controls represent categories of rock–mass conditions rather than detailed block-scale geometries. Future developments will focus on extending the model to three dimensions incorporating lateral

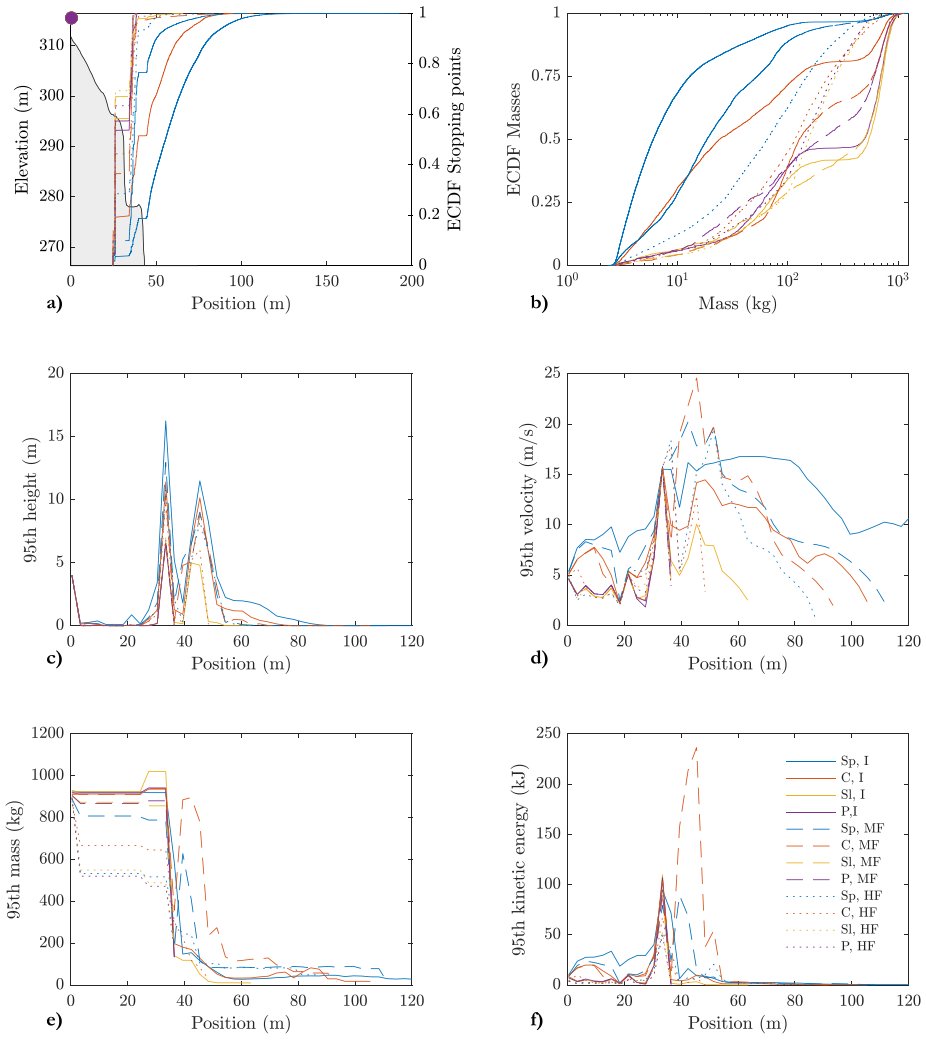


Fig. 11. Sensitivity analysis for different block shapes (sphere, cube, slab, prism) and rock–mass conditions (intact, moderately fractured, highly fractured). Abbreviations: Sp = sphere, C = cube, Sl = slab, P = prism; I = intact, MF = moderately fractured, HF = highly fractured. Results are presented as: (a) empirical cumulative distribution functions (ECDFs) of stopping positions; (b) ECDFs of block or fragment masses; (c)–(f) spatial evolution of the 95th percentile of trajectory height, velocity, mass and kinetic energy, respectively. For clarity, the x-axis is truncated at 120 m to enhance visibility of the main deposit zone; however, the Sp–I (sphere, intact) configuration reaches runout distances up to 192 m.

dispersion in a probabilistic framework, based on experimental observations. Additional efforts will aim to refine the treatment of fragment shape and internal structure, and expanding both laboratory and field datasets for calibration and validation. Finally, future studies will focus on extending the framework to incorporate fracture-mechanics-based size-effect laws, potentially combined with a rate-dependent treatment and applied across a wider range of block sizes and lithologies. These enhancements will further improve the predictive capability of RockFRAG and its applicability to site-specific hazard assessments in complex geological settings.

Open access

This article is licensed under a Creative Commons Attribution 4.0 International License, which permits use, sharing, adaptation, distribution and reproduction in any medium or format, as long as you give appropriate credit to the original author(s) and the source, provide a link to the Creative Commons licence, and indicate if changes were made. The images or other third party material in this article are included in the article's Creative Commons licence, unless indicated otherwise in a credit line to the material. If material is not included in the article's Creative Commons licence and your intended use is not permitted by statutory regulation or exceeds the permitted use, you will need to obtain permission directly from the copyright holder. To view a copy of this licence, visit http://creativecommons.org/licenses/by/4.0/.

Funding

This work was supported by Marie Curie Postdoctoral Fellowship 2022 (Call Horizon-MSCA-2022-PF-01, grant GA101103401 - RIDETHERISK project).

Declaration of competing interest

The authors declare that they have no known competing financial interests or personal relationships that could have appeared to influence the work reported in this paper.

Appendix A. Comparative analysis of trajectory models incorporating fragmentation

See Table A.17.

Table A.17
Comparison of rockfall fragmentation and trajectory models: attributes vs. models. Symbols and notation follow the *List of Abbreviations* (e.g., ϕ for friction angle) to ensure consistency and avoid language ambiguity. References: RockGIS[8,9,11,121]; HY–Stone[17–20,122]; NURock.[24]

Attribute	RockGIS	HY-Stone	NURock	RockFRAG (Proposed)
General model				
Block-shape model	Hybrid: Lumped-mass (latest code: spherical at rebound only)	Hybrid: Lumped-mass (simplified-shape options for some specific impact submodels)	Lumped-mass (spherical for the only version without fragmentation)	Lumped-mass (shape class used parametrically for COR_n and Fragmentation module: sphere, cube, slab, prism)
Block type of motions	Free fall, bouncing.	Free fall, bouncing, rolling/sliding;	Free fall, bouncing, sliding;	Free fall, bouncing, sliding.
Kinematic Components Included	Translation, rotation	Translation, rotation	Translation (rotation in the code without fragmentation, only)	Translation
Dimensionality	3D	3D	2.5D	2D (3D planned)
Block-related inputs	m, d_{eq}, $x_{0,B}$, $y_{0,B}$, $z_{0,B}$, $v_{0,B}$&$\omega_{0,B}$ (x, y, z components)	m, d_{eq}, $x_{0,B}$, $y_{0,B}$, $z_{0,B}$, $v_{0,B}$&$\omega_{0,B}$ (x, y, z components)	m, d_{eq}, $x_{0,B}$, $y_{0,B}$, $z_{0,B}$, $v_{0,B}$ (x, y, z components)	m, d_{eq}, $x_{0,B}$, $y_{0,B}$, $v_{0,B}$ (x, y components)
Slope or block–slope related inputs	DEM/DTM, $COR_n = f$(substrate type, i), $COR_t = f$(deformation energies, d_{eq}, v_n)	DEM/DTM, $COR_n = f$(substrate type) and $COR_t = f$(substrate type), rolling friction angle ϕ_r	DEM/DTM, $COR_n = f$(substrate type) and $COR_t = f$(substrate type), ϕ	DEM/DTM, $COR_n = f$(substrate type, v^a and i, block shape and size), $COR_t = f$(substrate type), ϕ.
Fragmentation model				
Fragmentation starting criterion	1st version[8]: Empirical survival rate; 2st version[11]: Energy-based threshold calibrated by investigated sites; later formulation (not yet implemented)[13]: functional formulation $F = f(m$, block shape, σ_c, E_k^a, ι, contact geometry, substrate type, internal block structure) calibrated from full-scale tests.	Weibull-type energy threshold[21] depending on block material properties, geometrical characteristics and impact velocity.	Stochastic survival probability depending on block material properties, geometrical characteristics and impact velocity.	Energy-based threshold[123] corrected for shape and rock mass condition depending on block material properties, geometrical characteristics and impact velocity with probabilistic structural control.
Fragment size distribution	Power-law distribution (1st version: fixed parameters, 1st version: $f(v^a, m)$	Power-law distribution with fixed parameter	Empirical formulation based on drop tests on intact spheres	Bilinear ECDF, dependent on rock–mass condition and on the impact-energy ratio over the fragmentation threshold energy, fitted from drop tests on spheres with& without discontinuities and on simplified-shape specimens.
Fragment motion treatment	Fixed-cone stochastic ejection; % energy loss from literature; energy $\propto$ fragment mass.	Fixed-cone stochastic ejection; no energy loss for fragmentation (momentum conservation criteria); energy $\propto$ fragment mass with model parameter.	Probabilistic velocity vectors, empirical α and a stochastic azimuth angle (based on drop tests on intact spheres); energy loss due to fragmentation is a function of the fracture area; energy $\propto$ fragment mass; the tangential component includes $v_{b,t}\,\mathrm{COR}_t$.	Probabilistic velocity vectors; empirical α function of rock–mass condition and θ (based on drop tests on spheres with& without discontinuities and on simplified-shape specimens), energy $\propto$ fragment mass; the tangential component includes $v_{b,t}\,\mathrm{COR}_t$.
Input parameters	m, d_{eq}, survival probability $q = f(q_1, q_2)$ and proportion between the fragment size generated and the initial volume $b = f(b_1, b_2)$ (q and b depend also of impact condition and they are used to compute largest generated fragment size and fractal dimension), model parameters a_1, a_2, minimum volume of the fragment generated, angle of aperture of the ejection cone.	m, d_{eq}, Y_B, Y_s ν_B, ν_s, σ_c, maximum fragment size, Weibull parameter, model parameter for the power-law, angle of aperture of the ejection cone, model-parameter for fragments energy.	m, d_{eq}, Y_B, Y_s ν_B, ν_s, σ_c, σ_t (from Brazilian test BT), Diameter of specimen used for BT, Critical Force (from BT), Weibull shape parameter pertaining to the distribution of maximum force under BT, Critical value of work required to fail a disc under BT, Weibull shape parameter pertaining to the distribution of work required to fail discs under BT, Mode I fracture toughness.	V_B, ϕ Y_B, Y_s ν_B, ν_s, σ_t, shape (4 classes), rock mass condition (3 classes), V_{th}, m_{th}

(*continued on next page*)

Table A.17 (*continued*).

Main limitations/notes	Spherical blocks assumption; no explicit discontinuity control; fixed-cone oversimplifies dispersion; several user-defined site-specific parameters (to be calibrated); scale-variant factor applicable (but not yet applied) for defining the number of fragment.	Spherical blocks assumption; no explicit discontinuity control; fixed-cone oversimplifies dispersion; several user-defined site-specific parameters (to be calibrated); scale-invariant fracture-mechanics; no field validation.	Spherical blocks assumption; no explicit discontinuity control; limited lateral dispersion/rotation; scale-invariant fracture-mechanics; field validation promising but limited.	Current 2D (no explicit lateral dispersion) and no rotation; discontinuity network not explicit (orientation handled probabilistically); fragments inheriting parent properties; scale-invariant fracture-mechanics.
Main Pros	Includes rotation and 3D kinematics; suitable for regional-scale assessments; extensive field calibration.	Includes 3D kinematics; suitable for regional-scale assessments.	Includes 3D kinematics; suitable for regional-scale assessments; laboratory-calibrated formulas (drop tests on intact spheres); probabilistic velocity vectors; includes damage accumulation for intact blocks.	Suitable for regional-scale assessments; integrates shape variability; integrates rock–mass structural condition; laboratory-calibrated formulas (drop tests on spheres with& without discontinuities and on simplified-shape specimens); probabilistic velocity vectors;

Table B.18
Input parameters adopted in the worked example, reported as mean values and associated standard deviations used for Monte Carlo sampling. For this worked example, the normal coefficient of restitution is assumed equal to the base value, i.e. $COR_n = COR_{n0}$.

Category	Parameter	Mean value	Std. dev.
Block geometry and structural condition	Block volume, V_B (m^3)	1.0	0.1
	Block shape	Cube	–
	Rock mass condition	Moderately fractured	–
Block material	Density, ρ ($kg\,m^{-3}$)	2700	30
	Tensile strength, σ_t (MPa)	7.0	0.7
	Young's modulus, Y_B (GPa)	80	8
	Poisson's ratio, ν_B (–)	0.20	0.02
Block fragments threshold	Minimum fragment mass threshold m_{th} (kg)	0.5	–
	Threshold fragment volumeV_{th} (m^3)	0.0	–
Slope material	Young's modulus, Y_s (GPa)	80	8
	Poisson's ratio, ν_s (–)	0.20	0.02
	Friction angle, ϕ (°)	30	3
Block–slope interaction parameters	Normal restitution coefficient COR_n (–)	0.30	0.03
	Tangential restitution coefficient COR_t (–)	0.70	0.07
Impact kinematics	Normal velocity, $v_{b,n}$ ($m\,s^{-1}$)	3.0	–
	Tangential velocity, $v_{b,t}$ ($m\,s^{-1}$)	1.0	–

Appendix B. Worked example of a single impact with fragmentation

This appendix provides a worked example of a single impact event with fragmentation, aimed at illustrating how the governing equations of the RockFRAG framework are combined within a single calculation workflow. The purpose of this example is purely illustrative and did not represent a full trajectory simulation. In the present example, initial block conditions such as release position, trajectory, and pre-impact motion are not defined. Instead, the impact kinematics are prescribed directly in terms of the normal and tangential components of the translational velocity at impact. This allows the fragmentation procedure and the post-impact fragment kinematics to be demonstrated independently of the trajectory computation. Table B.18 summarises the input parameters adopted in the worked example. Mean values of the material, geometric, and interaction parameters are used, and where applicable, standard deviations indicate the uncertainty ranges employed in Monte Carlo sampling. For the purpose of this worked example, all fragments generated upon impact are assumed to inherit the rock–mass structural condition of the parent block. Accordingly, the threshold fragment volume governing the transition from moderately fractured to intact behaviour is set to $V_{th} = 0\ m^3$, so that no scale-dependent reclassification of fragment structural condition is applied in this example.

The example refers to one Monte Carlo realisation extracted from a simulation set of N_{sim} trials; in the reported case, mean values of the input parameters are sampled. For the selected Monte Carlo realisation, the discontinuity inclination θ is randomly extracted and equal to $\theta = 80°$. According to the orientation-dependent strength reduction described in Section 3.1, this results in an effective tensile strength $\tilde{\sigma}_t = 4.55$ MPa. The fragmentation threshold energy E_{th} is computed according to Eq. (2), using the equivalent diameter d_{eq} derived from the initial block volume and the shape-dependent correction factor $k_{s,E_{th}}$ equal to 2, yielding $E_{th} = 4.96$ kJ. The normal component of the translational kinetic energy at impact is then computed as: $E^b_{k_{t,n}} = \frac{1}{2} m v^2_{b,n} = 12.15$ kJ. According to Eq. (5), the corresponding energy ratio is: $\epsilon = E^b_{k_{t,n}} / E_{th} = 2.45$, indicating that fragmentation is triggered.

Once fragmentation occurs, fragment masses are sampled via Monte Carlo extraction from the empirical complementary cumulative distribution function corresponding to the moderately fractured rock–mass class and the computed energy ratio. For $\epsilon = 2.45$ and a moderately fractured rock mass, the bilinear parameters of the complementary cumulative fragment-size distribution are computed from the fitted expressions reported in Table 4, resulting in: B = 1.398, C = −0.855, and D = 1.711. Sampling proceeds iteratively while enforcing mass conservation, until the sum of the generated fragment masses equals the mass of the parent block. For this realisation, the generated fragment

volumes (in m^3) are: 0.0185, 0.0981, 0.3432, 0.5392 m^3, whose sum equals the parent block volume of 1 m^3.

For each generated fragment, the scaling factor ψ is sampled from the distribution reported in Table 6, yielding $\psi = 0.98$, and the effective restitution coefficient $COR_{,i}$ is then calculated according to Eq. (8). The fragment ejection angle α is then sampled from the experimentally derived bounds reported in Fig. 4. A value $\alpha = 17.51°$ is obtained. The post-impact velocity components of the fragment are then computed using Eqs. (10)–(11), resulting in: $v^a_{f,t} = 0.90\ m\,s^{-1}$, and $v^a_{f,n} = 0.86\ m\,s^{-1}$.

Each fragment generated in this single impact is subsequently treated as a new block for propagation purposes, inheriting the mechanical and structural properties of the parent block, consistently with the assumptions of the present example. The procedure illustrated herein corresponds to one Monte Carlo realisation within the broader probabilistic framework and is representative of the calculations performed at each impact location during a full simulation, following the workflow shown in Figs. 1 and 2.

Appendix C. Consistency check using the Omells rockfall case

An additional consistency check was performed using the Omells rockfall case reported by Ruiz-Carulla and Corominas[11] and Ruiz-Carulla et al.,[124] for which fragmentation data from a natural event are available in terms of detached and deposited total volumes, number of detached blocks, and number of deposited fragments. The objective of this appendix is not to provide a full trajectory validation, which would require detailed information on impact locations, kinematics and block–slope interaction parameters, but rather to assess whether the proposed fragmentation-aware framework is consistent with field-scale observations from a documented natural rockfall.

At the Omells site, an initial volume of approximately 4.2 m^3, interpreted as corresponding to an almost single block, given a maximum individual block volume of about 4 m^3, resulted in 48 fragments, with measured fragment volumes ranging from approximately 1.1 m^3 down to 7×10^{-4} m^3.[11] Based on the reconstruction proposed by Ruiz-Carulla and Corominas,[11] the first fragmentation is hypothesised to have occurred after an impact following a fall height of approximately 1 m, corresponding to an impact velocity of 4.42 m s^{-1}. In addition to fragmentation statistics, qualitative runout information can also be extracted from the Omells case. The rockfall developed along a stepped slope profile, characterised by a downslope by softer ground conditions. According to Ruiz-Carulla et al.,[124] the block exhibiting the maximum runout was stopped after impacting a wall located approximately 22–23 m downslope from the source area. When represented along a simplified two-dimensional topographic profile representative of the most probable block path, as reported by Ruiz-Carulla et al.,[124] this corresponds to a horizontal distance of approximately $x \approx 30$ m (Fig. C.12). A rockfall barrier located $x \approx 23$ m was impacted as well. In contrast, several other blocks, including the largest observed fragment, stopped significantly closer to the source area, at distances ranging between approximately 10 and 13 m. The fact that the largest fragment stopped at relatively short distance strongly suggests that it was generated during an early impact, most likely the first one.

Using the mechanical properties reported by Ruiz-Carulla et al.[124] (density 2350 kg m^{-3}, tensile strength 2.03 MPa, Young's modulus 5185 MPa, and Poisson's ratio 0.006), and assuming a moderately fractured rock mass condition consistent with the reported RMR $\approx$ 64, the fragmentation threshold energy E_{th} was evaluated according to Eq. (2). A total of 1000 Monte Carlo realisations were performed to account solely for uncertainty in discontinuity orientation and the resulting variability in E_{th} and in the fragment-size distribution parameters. Considering only the first impact and neglecting subsequent interactions, the median value of the largest fragment generated by the simulations was 1.05 m^3, in very close agreement with the observed maximum fragment volume of 1.1 m^3.

To explore run-out aspect within the proposed framework, despite in a qualitative way, the two-dimensional topographic profile and a stepped soft-ground condition downstream of the rock slope reported in[124] were considered. Accordingly, mean values of the normal and tangential coefficients of restitution equal to $COR_n = 0.3$ and $COR_t = 0.6$ respectively, were used and considered representative of block–soil interactions. Fig. C.12 shows the empirical cumulative distribution function (ECDF) of simulated stopping distances along the profile. Two preferential accumulation zones emerge, at approximately $x \approx 13$ m and $x \approx 30$ m. These locations closely correspond to the stopping distances documented in the Omells case, namely: (i) short runouts associated with early fragmentation products, including the largest block, and (ii) longer runouts associated with blocks reaching and impacting the retaining wall or barrier system.

Although the comparison remains qualitative and does not allow full trajectory validation, the ability of the model to reproduce both the observed fragmentation scale and the bimodal distribution of stopping distances provides a consistency check at field scale.

Appendix D. Convergence and consistency of fragmentation simulations

Fragmentation in RockFRAG is simulated through a Monte Carlo approach; consequently, the number, size and trajectories of generated fragments vary between individual realisations. The objective of the simulations is therefore not to reproduce a single deterministic trajectory, but to obtain statistically representative distributions of rockfall response parameters relevant for hazard and risk assessment. In this context, model consistency is evaluated by analysing the convergence of probabilistic indicators as the number of simulations N_{sim} increases. For rockfall applications, such indicators typically include: (i) the empirical cumulative distribution of stopping points (runout), (ii) the empirical cumulative distribution of fragment masses, and (iii) the spatial evolution along the slope of characteristic percentile values (here the 95th percentile) of trajectory height, velocity and kinetic energy.

To illustrate this aspect, a convergence analysis is reported for the Vallirana Site 4 case (after Matas et al.[9]), which is used in Section 4 to validate fragment runout distributions. The same scenario was simulated using $N_{sim} = 10$, 100, 500 and 1000 realisations, while keeping all other input parameters unchanged. Results are considered converged when the relative variation of probabilistic indicators between successive simulation batches is below 1%.

Fig. D.13 compares the resulting outputs. For low numbers of simulations (10 and 100), noticeable scatter is observed, particularly in percentile-based profiles. However, the curves rapidly stabilise as N_{sim} increases. For $N_{sim} \geq 500$, no significant differences are observed in the runout ECDF, fragment mass distribution, or in the spatial trends of the 95th percentile of trajectory height and kinetic energy. Small local discrepancies visible in the velocity percentile are associated with isolated trajectories and represent very low exceedance probabilities; from a hazard-assessment perspective, these effects are negligible.

This analysis indicates that a number of simulations greater than approximately 500 is sufficient to ensure statistically stable and representative results for fragmentation-driven rockfall scenarios. Accordingly, the values of N_{sim} adopted throughout this study guarantee robustness of the probabilistic outputs used for model validation and hazard interpretation.

Data availability

Data will be made available on request.

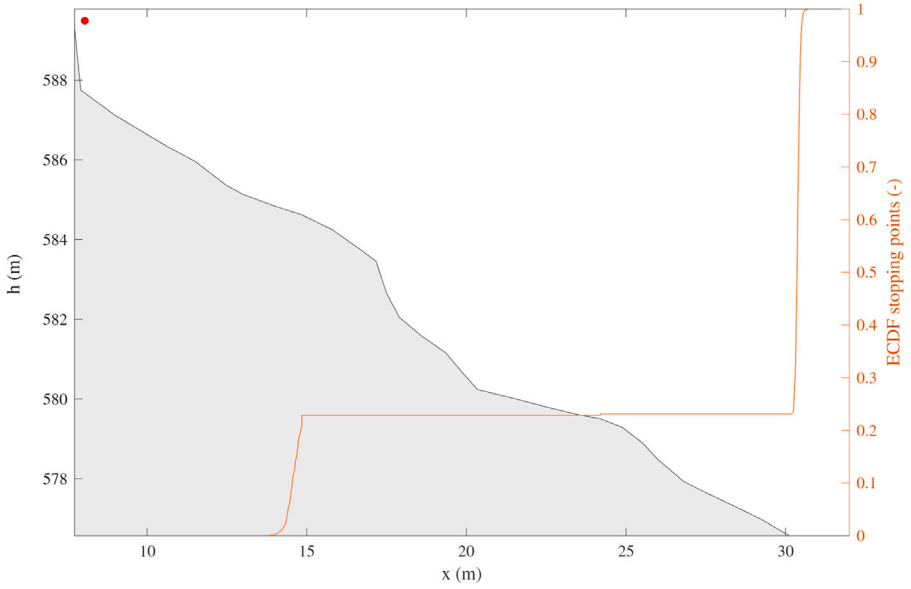


Fig. C.12. Empirical cumulative distribution function (ECDF) of simulated block stopping points for the Omells rockfall case.[124] The black line represents the two-dimensional topographic profile. The release point is shown in red.

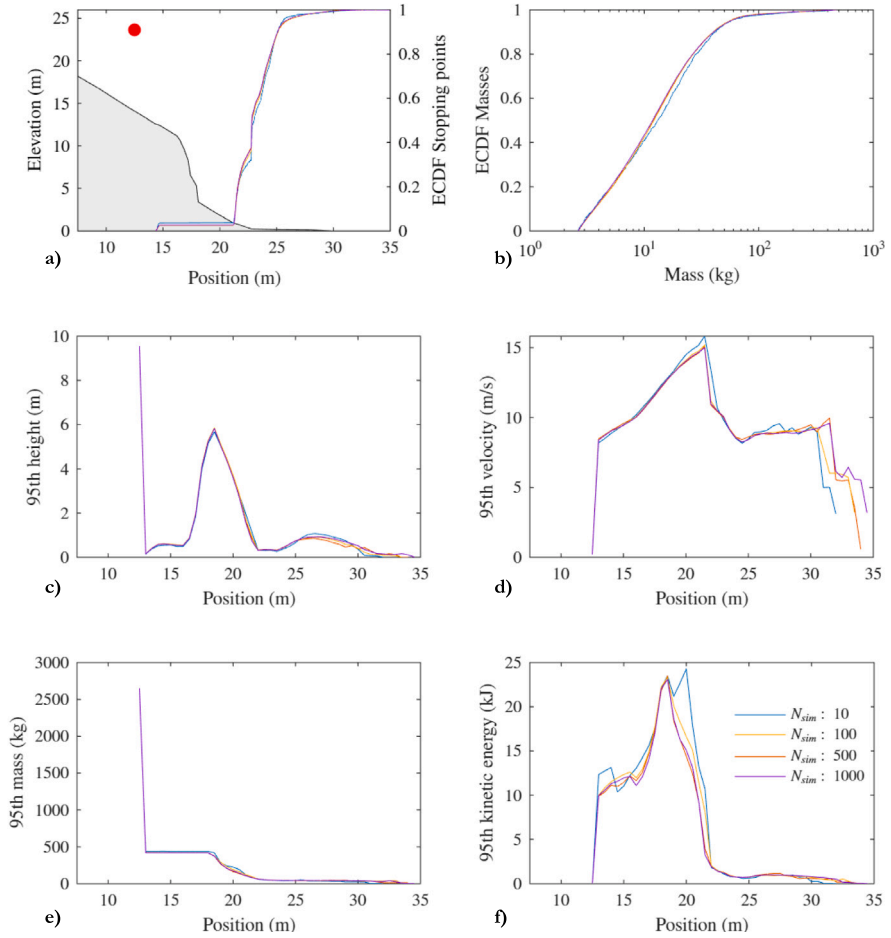


Fig. D.13. Convergence analysis of fragmentation simulations for the Vallirana Site 4 case. Comparison of results obtained with N_{sim} = 10, 100, 500 and 1000 simulations: (a) empirical cumulative distribution of stopping points (runout). The release point is shown in red; (b) empirical cumulative distribution of fragment masses; (c) spatial evolution of the 95th percentile of trajectory height; (d) spatial evolution of the 95th percentile of trajectory velocity; (e) spatial evolution of the 95th percentile of fragment mass; (f) spatial evolution of the 95th percentile of kinetic energy.

References

1. Scavia Claudio, Barbero Monica, Castelli Marta, Marchelli Maddalena, Peila Daniele, Torsello Giulia, Vallero Gianmarco. Evaluating rockfall risk: Some critical aspects. *Geosciences*. 2020;10(3):98.
2. Hantz Didier, Corominas Jordi, Crosta Giovanni B, Jaboyedoff Michel. Definitions and concepts for quantitative rockfall hazard and risk analysis. *Geosciences*. 2021;11(4):158.
3. Rosser Nick, Massey Chris. Rockfall hazard and risk. In: *Landslide Hazards, Risks, and Disasters*. Elsevier; 2022:581–622.
4. Lin Qiwen, Cheng Qiangong, Li Kun, Xie Yu, Wang Yufeng. Contributions of rock mass structure to the emplacement of fragmenting rockfalls and rockslides: insights from laboratory experiments. *J Geophys Res: Solid Earth*. 2020;125(4):e2019JB019296.
5. Corominas Jordi, Mavrouli Olga, Ruiz-Carulla Roger. Rockfall occurrence and fragmentation. In: *Advancing Culture of Living with Landslides: Volume 1 ISDR-ICL Sendai Partnerships 2015-2025*. Springer; 2017:75–97.
6. De Blasio Fabio Vittorio, Crosta Giovanni Battista. Fragmentation and boosting of rock falls and rock avalanches. *Geophys Res Lett*. 2015;42(20):8463–8470.
7. Zhao Tao, Crosta Giovanni Battista, Utili Stefano, De Blasio Fabio Vittorio. Investigation of rock fragmentation during rockfalls and rock avalanches via 3-D discrete element analyses. *J Geophys Res: Earth Surf*. 2017;122(3):678–695.
8. Matas Gerard, Lantada Nieves, Corominas Jordi, Gili Josep A, Ruiz-Carulla Roger, Prades Albert. RockGIS: a GIS-based model for the analysis of fragmentation in rockfalls. *Landslides*. 2017;14(5):1565–1578.
9. Matas Gerard, Lantada Nieves, Corominas Jordi, Gili Josep, Ruiz-Carulla Roger, Prades Albert. Simulation of full-scale rockfall tests with a fragmentation model. *Geosciences*. 2020;10(5):168.
10. Ruiz-Carulla Roger, Corominas Jordi, Mavrouli Olga. A fractal fragmentation model for rockfalls. *Landslides*. 2017;14(3):875–889.
11. Ruiz-Carulla Roger, Corominas Jordi. Analysis of rockfalls by means of a fractal fragmentation model. *Rock Mech Rock Eng*. 2020;53(3):1433–1455.
12. Perfect E. Fractal models for the fragmentation of rocks and soils: a review. *Eng Geol*. 1997;48(3–4):185–198.
13. Gili Josep A, Ruiz-Carulla Roger, Matas G, Moya J, Prades A, Corominas J, Lantada Nieves, Núñez Andrés María Amparo, Buill F, Puig C, et al. Rockfalls: Analysis of the block fragmentation through field experiments. *Landslides*. 2022;19(5):1009–1029.
14. Wang Yuannian, Tonon Fulvio, Crosta Giovanni Battista, Agliardi Federico, Zavodni ZM. Rock fragmentation module in 3-D rock-fall analysis. In: *ARMA US Rock Mechanics/Geomechanics Symposium*. ARMA; 2010:ARMA–10.
15. Wang Yuannian, Tonon Fulvio. Discrete element modeling of rock fragmentation upon impact in rock fall analysis. *Rock Mech Rock Eng*. 2011;44:23–35.
16. Wang Yuannian, Tonon Fulvio. Dynamic validation of a discrete element code in modeling rock fragmentation. *Int J Rock Mech Min Sci*. 2011;48(4):535–545.
17. Frattini Paolo, Crosta Giovanni Battista, Agliardi Federico, et al. Rockfall characterization and modeling. In: *Landslides Types, Mechanisms and Modeling*. Cambridge University Press; 2012:267–281.
18. Dattola Giuseppe, Crosta Giovanni Battista, di Prisco Claudio. Investigating the influence of block rotation and shape on the impact process. *Int J Rock Mech Min Sci*. 2021;147:104867.
19. Lanfranconi Camilla, Frattini Paolo, Sala Gianluca, Dattola Giuseppe, Bertolo Davide, Sun Juanjuan, Crosta Giovanni Battista. Accounting for the effect of forest and fragmentation in probabilistic rockfall hazard. *Nat Hazards Earth Syst Sci*. 2023;23(6):2349–2363.
20. Crosta GB, Agliardi F. Parametric evaluation of 3D dispersion of rockfall trajectories. *Nat Hazards Earth Syst Sci*. 2004;4(4):583–598.
21. Yashima S, Kanda Y, Sano S. Relationships between particle size and fracture energy or impact velocity required to fracture as estimated from single particle crushing. *Powder Technol*. 1987;51(3):277–282.
22. Marchelli Maddalena, Guccione Davide Ettore, Giacomini Anna, Buzzi Olivier. Fragmentation patterns and trajectories during rockfall: Analysis of the influence of discontinuities and impact conditions through drop tests. *Rock Mech Rock Eng*. 2025:1–33.
23. Zhao Yongjie, Wu Yong, Wang Yingpeng, He Siming, Li Xinpo, Zhu Lei, Wang Zhangqing. Study on the influence of 3D pre-existing joint on rockfall fragmentation during impact based on discrete element method. *Comput Geotech*. 2025;184:107270.
24. Guccione Davide Ettore, Barros Guilherme, Thoeni Klaus, Huang Zhanyu, Giacomini Anna, Buzzi Olivier. A new stochastic rockfall fragmentation approach for lumped mass simulations. *Rock Mech Rock Eng*. 2025:1–34.
25. Dussauge Carine, Grasso Jean-Robert, Helmstetter Agnès. Statistical analysis of rockfall volume distributions: Implications for rockfall dynamics. *J Geophys Res: Solid Earth*. 2003;108(B6).
26. Hantz D, Ventroux Q, Rossetti JP, Berger F. A new approach of diffuse rockfall hazard. In: *Landslides and Engineered Slopes. Experience, Theory and Practice*. CRC Press; 2018:1063–1067.
27. Lanfranconi Camilla, Frattini Paolo, Agliardi Federico, Stock Greg M, Collins Brian D, Crosta Giovanni. Field evidence and indicators of rockfall fragmentation and implications for mobility. *Eng Geol*. 2024;341:107704.
28. Carmona Humberto A, Wittel Falk K, Kun Ferenc, Herrmann Hans Jürgen. Fragmentation processes in impact of spheres. *Phys Rev E—Stat Nonlinear Soft Matter Phys*. 2008;77(5):051302.
29. Wittel Falk K, Carmona Humberto A, Kun Ferenc, Herrmann Hans J. Mechanisms in impact fragmentation. *Int J Fract*. 2008;154:105–117.
30. Marchelli Maddalena, Guccione Davide Ettore, Giacomini Anna, Buzzi Olivier. Fragmentation and energy dissipation in rockfall: Effects of block shape and non-collinear impact dynamics. *Int J Rock Mech Min Sci*. 2026;198:106381.
31. Zhang Kai, Zhang Ke, Ye Jinmin, Liu Wenlian, Guan Shihao, Li Na. Cracking and deformation behaviors of overhanging rock: Laboratory tests and optical monitoring. *J Rock Mech Geotech Eng*. 2025;17(7):4077–4097.
32. Dorren Luuk, Berger Frederic, Putters US. Real-size experiments and 3-D simulation of rockfall on forested and non-forested slopes. *Nat Hazards Earth Syst Sci*. 2006;6(1):145–153.
33. Dorren Luuk, Berger Frédéric, Bourrier Franck, Eckert Nicolas, Saroglou Charalampos, Schwarz Massimiliano, Stoffel Markus, Trappmann Daniel, Utelli Hans-Heini, Moos Christine. Delimiting rockfall runout zones using reach probability values simulated with a Monte-Carlo based 3D trajectory model. *Nat Hazards Earth Syst Sci Discuss*. 2022:1–23.
34. Ashayer Parham. *Application of Rigid Body Impact Mechanics and Discrete Element Modeling to Rockfall Simulation* [Phd thesis]. University of Toronto; 2007.
35. Bourrier Franck, Berger Frédéric, Tardif Pascal, Dorren Luuk, Hungr Oldrich. Rockfall rebound: comparison of detailed field experiments and alternative modelling approaches. *Earth Surf Process Landf*. 2012;37(6):656–665.
36. Leine Remco I, Schweizer Andreas, Christen Marc, Glover James, Bartelt P, Gerber Werner. Simulation of rockfall trajectories with consideration of rock shape. *Multibody Syst Dyn*. 2014;32:241–271.
37. Leine Remco I, Capobianco Giuseppe, Bartelt Perry, Christen Marc, Caviezel Andrin. Stability of rigid body motion through an extended intermediate axis theorem: application to rockfall simulation. *Multibody Syst Dyn*. 2021;52(4):431–455.
38. Bourrier Franck, Acary Vincent. Predictive capabilities of 2D and 3D block propagation models integrating block shape assessed from field experiments. *Rock Mech Rock Eng*. 2022;55(2):591–609.
39. Dhiman Raj Kiran, Bourrier Franck, Thakur Mahesh. A new rockfall propagation model: Examining rockfall risk in Manikaran, NW Himalaya, India. In: *XIVth International Symposium on Landslides*. 2024.
40. Garcia B, Villard Pascal, Richefeu V, Daudon D. Comparison of full-scale rockfall tests with 3D complex-shaped discrete element simulations. *Eng Geol*. 2022;310:106855.
41. Ma Ke, Liu Guoyang. Three-dimensional discontinuous deformation analysis of failure mechanisms and movement characteristics of slope rockfalls. *Rock Mech Rock Eng*. 2022;55(1):275–296.
42. Liu Guoyang, Kang Jiashuo, Ye Tangjin, Wang Shuonan, Bo Wu, Duoji Danzhen, Tian Yongxin. Three-dimensional (3D) laser scanning–based identification of rock mass discontinuities for rockfall modeling using 3D discontinuous deformation analysis. *Int J Rock Mech Min Sci*. 2026;202:106484.
43. Wu Maolin, Luo Gang, Hu Xiewen, Bi Yuzhang, Wang Yufeng, Ma Ning. Dynamic fragmentation analysis of potential rockfall hazards at Zixia hydropower dam, Qinghai-Tibet plateau. *J Rock Mech Geotech Eng*. 2025;17:4109–4123.
44. Zhang Wen, Wang Yaoyao, Chen Junqi, Wang Jia, Liu Qing, Yin Han, Zhao Xiaohan. Kinetic analysis of rockfall blocks considering fragmentation effects for high and steep slopes. *Comput Geotech*. 2025;187:107482.
45. Marchelli Maddalena, De Biagi Valerio, Paganone Marco, Bertolo Davide. A hybrid approach to quantifying rockfall risk with limited knowledge: a case study in Aosta Valley. *Bull Eng Geol Environ*. 2025;84(11):1–21.
46. Li Langping, Lan Hengxing. Probabilistic modeling of rockfall trajectories: a review. *Bull Eng Geol Environ*. 2015;74:1163–1176.
47. The MathWorks Inc. *MATLAB Version: 9.13.0 (R2023b)*. Natick, Massachusetts, United States: The MathWorks Inc.; 2023 URL https://www.mathworks.com.
48. RocScience Inc. RocFall, user's guide. 1998–2002.
49. Marchelli Maddalena, Peila Daniele, Giacomini Anna. Rockfall in open pit mines: management of the pit geometry and protection measures design. *Int J Rock Mech Min Sci*. 2023;170:105551.
50. Barton Nicholas, Lien Reidar, Lunde JJRM. Engineering classification of rock masses for the design of tunnel support. *Rock Mech*. 1974;6(4):189–236.
51. Bieniawski ZT. *Engineering Rock Mass Classifications: A Complete Manual for Engineers and Geologists in Mining, Civil and Petroleum Engineering*. Chichester: John Wiley & Sons; 1989.
52. Hoek E, Carranza-Torres C, Corkum B. Hoek–brown failure criterion – 2002 edition. In: *Proceedings of the NARMS-TAC Conference*. Toronto: Canadian Rock Mechanics Association; 2002:267–273.
53. Saroglou Charalampos. The challenge of rock mass classification of anisotropic rockmasses. *Rock Mech Rock Eng*. 2025:1–21.
54. Schlotfeldt P, Carter TG. A new and unified approach to improved scalability and volumetric fracture intensity quantification for GSI and rockmass strength and deformability estimation. *Int J Rock Mech Min Sci*. 2018;110:48–67.
55. Pantelidis Lysandros. Rock slope stability assessment through rock mass classification systems. *Int J Rock Mech Min Sci*. 2009;46(2):315–325.

56. Jaiswal Amit, Verma AK, Singh TN. A critical review of rock mass classification systems for assessing the stability condition of rock slopes. *Environ Earth Sci*. 2024;83(8):245.
57. Corominas Jordi, Matas Gerard, Ruiz-Carulla Roger. Quantitative risk analysis of fragmental rockfalls: A case study. In: *ISRM EUROCK*. ISRM; 2018:ISRM–EUROCK.
58. Zhang Qian Bing, Zhao Jian. Quasi-static and dynamic fracture behaviour of rock materials: phenomena and mechanisms. *Int J Fract*. 2014;189(1):1–32.
59. Choanji Tiggi, Jaboyedoff Michel, Yuskar Yuniarti, Samsu Anindita, Fei Li, Derron Marc-Henri. Evolution of rockfall based on structure from motion reconstruction of street view imagery and unmanned aerial vehicle data: Case study from koto Panjang, Indonesia. *Remote Sens*. 2025;17(11):1888.
60. Bažant Zdeněk P, Planas Jaime. *Fracture and Size Effect in Concrete and Other Quasibrittle Materials*. New York: CRC Press / Routledge; 1998 http://dx.doi.org/10.1201/9780203756799, Comprehensive monograph on quasibrittle fracture, FPZ and size effect.
61. Jensen Stina Stokmo. *Experimental Study of Direct Tensile Strength in Sedimentary Rocks* [Master's thesis]. NTNU; 2016.
62. Zhou Changtai, Xie Heping, Zhu Jianbo. Revealing size effect and associated variability of rocks based on BPM–μ DFN modelling: significance of internal microstructure and strain rate. *Rock Mech Rock Eng*. 2024;57(4):2983–2996.
63. Pérez-Rey Ignacio, Muñoz-Ibáñez Andrea, González-Fernández Manuel A, Muñiz-Menéndez Mauro, Penabad Miguel Herbón, Estévez-Ventosa Xian, Delgado Jordi, Alejano Leandro R. Size effects on the tensile strength and fracture toughness of granitic rock in different tests. *J Rock Mech Geotech Eng*. 2023;15(9):2179–2192.
64. Jin Liu, Yu Wenxuan, Du Xiuli, Yang Wangxian. Dynamic size effect of concrete under tension: A numerical study. *Int J Impact Eng*. 2019;132:103318.
65. Liu Kai, Zou Chunjiang, Zhao Jian. Dynamic tensile behaviour of rocks under confining pressure and high-rate loadings. *Earth Energy Sci*. 2025;1(1):9–21.
66. Giacomini A, Buzzi O, Renard B, Giani GP. Experimental studies on fragmentation of rock falls on impact with rock surfaces. *Int J Rock Mech Min Sci*. 2009;46(4):708–715.
67. Ma Gang, Zhou Wei, Zhang Yida, Wang Qiao, Chang Xiaolin. Fractal behavior and shape characteristics of fragments produced by the impact of quasi-brittle spheres. *Powder Technol*. 2018;325:498–509. http://dx.doi.org/10.1016/j.powtec.2017.11.030.
68. Ma Gang, Wang Yihan, Zhou Heng, Lu Xi, Zhou Wei. Morphology characteristics of the fragments produced by rock grain crushing. *Int J Geomech*. 2022;22(4):04022020.
69. Grady Dennis E, Kipp Margaret E. Dynamic fracture and fragmentation. In: Asay JR, Shahinpoor M, eds. *High-Pressure Shock Compression of Solids*. New York: Springer; 1993:265–322. Describes dynamic crack growth, branching and interaction in fragmentation.
70. Zhang ZX, Kou SQ, Jiang LG, Lindqvist PA. Effects of loading rate on rock fracture: Fracture characteristics and energy partitioning. *Int J Rock Mech Min Sci*. 2000;37(5):745–762. http://dx.doi.org/10.1016/S1365-1609(00)00025-X.
71. Kou SQ, Lindqvist PA, Zhang ZX. Characterisation of crack propagation under dynamic loading in rock. *Eng Fract Mech*. 2000;65(1):109–119. http://dx.doi.org/10.1016/S0013-7944(99)00131-3.
72. Turcotte Donald L. Fractals and fragmentation. *J Geophys Res: Solid Earth*. 1986;91(B2):1921–1926. http://dx.doi.org/10.1029/JB091iB02p01921.
73. Perfect Edmund. Fractal models for the fragmentation of rocks and soils: A review. *Eng Geol*. 1997;48(3–4):185–198. http://dx.doi.org/10.1016/S0013-7952(97)00040-9.
74. Palmstrom Arild. The volumetric joint count–a useful and simple measure of the degree of rock mass jointing. In: *International Association of Engineering Geology. International Congress. 4*. 1982:221–228.
75. Giani Gian Paolo. *Rock Slope Stability Analysis*. Rotterdam: A. A. Balkema; 1992 ISBN 90-5410-026-2. Foundational treatment of structural control (joints/foliation) on slope failure mechanisms.
76. Ji Zhong-Min, Zhang Huan-Huan, Saroglou Haris, Asteriou Pavlos, Wang Ting-Hui, Wang Dong-Po, Wu Fa-Quan, Li Zhen-Hua. Three decades in review: The evolution of rockfall impact testing apparatuses. *Rock Mech Rock Eng*. 2025:1–26.
77. Losasso Lucia, Jaboyedoff Michel, Sdao Francesco. Potential rock fall source areas identification and rock fall propagation in the province of potenza territory using an empirically distributed approach. *Landslides*. 2017;14(5):1593–1602.
78. Marinos Paul, Hoek Evert. GSI: a geologically friendly tool for rock mass strength estimation. In: *ISRM International Symposium*. ISRM; 2000:ISRM–IS.
79. Marinos Paul G, Marinos Vassilis, Hoek Evert. The Geological Strength Index (GSI): A characterization tool for assessing engineering properties for rock masses. In: Romana M, Perucho Á, Olalla C, eds. *Underground Works Under Special Conditions*. London / Leiden / New York / Philadelphia / Singapore: Taylor & Francis / Balkema; 2007:13–21. In: Proceedings and Monographs in Engineering, Water and Earth Sciences;
80. Hoek Evert, Brown ET. The Hoek–Brown failure criterion and GSI–2018 edition. *J Rock Mech Geotech Eng*. 2019;11(3):445–463.
81. Sonmez H, Ulusay R. Modifications to the geological strength index (GSI) and their applicability to stability of slopes. *Int J Rock Mech Min Sci*. 1999;36(6):743–760.
82. Cai M, Kaiser PK, Uno H, Tasaka Y, Minami M. Estimation of rock mass deformation modulus and strength of jointed hard rock masses using the GSI system. *Int J Rock Mech Min Sci*. 2004;41(1):3–19. http://dx.doi.org/10.1016/S1365-1609(03)00025-X.
83. Schlotfeldt Paul, Carter T, Carter TG. A new and unified approach to improved scalability and volumetric fracture intensity quantification for GSI and rockmass strength and deformability estimation. *Int J Rock Mech Min Sci*. 2018;110:48–67. http://dx.doi.org/10.1016/j.ijrmms.2018.06.021.
84. Schlotfeldt Paul, Carvalho Jose, Panton Brad. Scale considerations and the quantification of the degree of fracturing for geological strength index (GSI) assessments. *Appl Sci*. 2025;15(15):8219.
85. Sonmez Harun, Dagdelenler Gulseren, Ozcelik Yilmaz, Ercanoglu Murat. A complementary approach to quantify the basic GSI chart considering scale effect on rock structure. *J Rock Mech Geotech Eng*. 2025;17(1):154–167.
86. Russo Andrea, Hormazábal Esteban. Correlations between various rock mass classification systems, including Laubscher (MRMR), Bieniawski (RMR), Barton (Q) and hoek and marinos (GSI) systems. In: *Geotechnical Engineering in the XXI Century: Lessons Learned and Future Challenges*. IOS Press; 2019:2806–2815.
87. Abbas N, Li KG, Emad MZ, Khan A. Quantifying uncertainty in rock mass properties: Implications for GSI, RMi, and RMR assessments. *J South Afr Inst Min Met*. 2024;124(5):285–291.
88. Asteriou Pavlos, Tsiambaos George. Effect of impact velocity, block mass and hardness on the coefficients of restitution for rockfall analysis. *Int J Rock Mech Min Sci*. 2018;106:41–50.
89. Ji Zhong-Min, Chen Zhi-Jian, Niu Qing-He, Wang Tian-Jun, Song Hao, Wang Ting-Hui. Laboratory study on the influencing factors and their control for the coefficient of restitution during rockfall impacts. *Landslides*. 2019;16(10):1939–1963.
90. Yang Xinzhi, Zhang Guangcheng, Yu Yi, Yu Qingtao, Lei Mengru, Ding Bingdong. Factors influencing the coefficient of restitution in rockfall impacts. *Nat Hazards Rev*. 2021;22(3):04021024.
91. Bi Ran, Li Shaoying, Liu Gou, Ren Jianxi, Song Yongjun. Investigating the effect of preimpact energy dissipation on coefficient of restitution regarding the slope-boulder interaction. *Adv Civ Eng*. 2021;2021(1):9929119.
92. Ferrari Federica, Giani Gian Paolo, Apuani Tiziana. Towards the comprehension of rockfall motion, with the aid of in situ tests. *Italian J Eng Geol Environ*. 2013:163–171.
93. Li Li-ping, Sun Shang-qu, Li Shu-cai, Zhang Qian-qing, Hu Cong, Shi Shao-shuai. Coefficient of restitution and kinetic energy loss of rockfall impacts. *KSCE J Civ Eng*. 2016;20:2297–2307.
94. Chau Kam Tim, Wong RHC, Liu J, Wu JJ, Lee CF. Shape effects on the coefficient of restitution during rockfall impacts. In: *ISRM Congress*. ISRM; 1999:ISRM–9CONGRESS.
95. Ferrari FEDERICA, Giani Gian Paolo, Apuani Tiziana, et al. Why can rockfall normal restitution coefficient be higher than one? *Rend Online Della Soc Geol Italiana*. 2013;24:122–124.
96. Ji Zhong-Min, Chen Zhi-Jian, Niu Qing-He, Wang Ting-Hui, Wang Tian-Jun, Chen Tian-Li. A calculation model of the normal coefficient of restitution based on multi-factor interaction experiments. *Landslides*. 2021;18(4):1531–1553.
97. Bi Ran, Han Zhao. Experimental investigation of the normal coefficient of restitution in rockfall collisions: Influence and interaction of controlling factors. *Appl Sci*. 2025;15(7):3874.
98. Wang Yanhai, Jiang Wei, Cheng Shengguo, Song Pengcheng, Mao Cong. Effects of the impact angle on the coefficient of restitution in rockfall analysis based on a medium-scale laboratory test. *Nat Hazards Earth Syst Sci*. 2018;18(11):3045–3061.
99. Asteriou Pavlos. Effect of impact angle and rotational motion of spherical blocks on the coefficients of restitution for rockfalls. *Geotech Geol Eng*. 2019;37(4):2523–2533.
100. Tang Jianhui, Zhou Xiaojun, Liang Kun, Lai Yalin, Zhou Gaofeng, Tan Jisheng. Experimental study on the coefficient of restitution for the rotational sphere rockfall. *Environ Earth Sci*. 2021;80(11):419.
101. Asteriou P, Saroglou H, Tsiambaos G. Geotechnical and kinematic parameters affecting the coefficients of restitution for rock fall analysis. *Int J Rock Mech Min Sci*. 2012;54:103–113.
102. Wang Nannan, Chen Fubang, Feng Aiguo. Research on normal restitution coefficient of rockfall collision. *Value Eng*. 2022;2(1).
103. Das Rajarshi, Cleary PW. Effect of rock shapes on brittle fracture using smoothed particle hydrodynamics. *Theor Appl Fract Mech*. 2010;53(1):47–60.
104. Marchelli Maddalena, Guccione Davide Ettore, Giacomini Anna, Buzzi Olivier. Fragmentation and energy dissipation in rockfall: effects of block shape and noncollinear impact dynamics. *Int J Rock Mech Min Sci*. 2026;198:106381.
105. Qin Sheng-Wu, Liu Xiao-Wei, Peng Shuai-Ying, Zhang Chao-Biao, Yao Jing-Yu, Lv Jiang-Feng, Wan Feng. Effect of rockfall shape on the coefficient of restitution: Insights from laboratory rockfall multi-parameter experiments. *Rock Mech Rock Eng*. 2026;59(1):855–879.
106. Ma Gang, Zhang Yida, Zhou Wei, Ng Tang-Tat, Wang Qiao, Chen Xing. The effect of different fracture mechanisms on impact fragmentation of brittle heterogeneous solid. *Int J Impact Eng*. 2018;113:132–143.

107. Tavares LM, King RP. Single-particle fracture under impact loading. *Int J Miner Process*. 1998;54(1):1–28.
108. Ma Tianshou, Peng Nian, Zhu Zhu, Zhang Qianbing, Yang Chunhe, Zhao Jian. Brazilian tensile strength of anisotropic rocks: review and new insights. *Energies*. 2018;11(2):304.
109. Han Dongya, Zhu Jianbo, Leung Yat-Fai. Failure strength and fracture characteristics of rock with discontinuity under indirect tension. *J Rock Mech Geotech Eng*. 2022;14(6):1810–1822.
110. Lee Youn-Kyou, Pietruszczak S. Tensile failure criterion for transversely isotropic rocks. *Int J Rock Mech Min Sci*. 2015;79:205–215.
111. Zhou Changtai, Rui Yichao, Qiu Jiadong, Wang Zhihe, Zhou Tao, Long Xiting, Shan Ke. The role of fracture in dynamic tensile responses of fractured rock mass: Insight from a particle-based model. *Int J Coal Sci Technol*. 2025;12(1):1–19.
112. Gili Josep A, Ruiz Carulla Roger, Matas Gerard, Corominas Jordi, Lantada Nieves, Núñez MA, Buill Felipe, Moya Jose, Prades A, Moreno S. Experimental study on rockfall fragmentation: In situ test design and first results. In: *Landslides and Engineered Slopes. Experience, Theory and Practice*. CRC Press; 2018:983–990.
113. Angelidakis Vasileios, Nadimi Sadegh, Utili Stefano. Elongation, flatness and compactness indices to characterise particle form. *Powder Technol*. 2022;396:689–695.
114. Guccione Davide Ettore, Giacomini Anna, Thoeni Klaus, Fityus Stephen, Buzzi Olivier. On the dynamic fragmentation of rock-like spheres: insights into fragment distribution and energy partition. *Rock Mech Rock Eng*. 2023;56(2):847–873.
115. Stronge William James. *Impact Mechanics*. Cambridge University Press; 2018.
116. De Biagi Valerio, Marchelli Maddalena, Peila Daniele. Reliability analysis and partial safety factors approach for rockfall protection structures. *Eng Struct*. 2020;213:110553.
117. Ruiz-Carulla Roger, Corominas Jordi, Gili Josep A, Matas Gerard, Lantada Nieves, Moya Jose, Prades Albert, Núñez Andrés María Amparo, Buill Felipe, Puig Carol. Analysis of fragmentation of rock blocks from real-scale tests. *Geosciences*. 2020;10(8):308.
118. Bourrier Franck, Toe David, Garcia Bruna, Baroth Julien, Lambert Stéphane. Experimental investigations on complex block propagation for the assessment of propagation models quality. *Landslides*. 2021;18(2):639–654.
119. Lei Qinghua, Latham J-P, Xiang Jiansheng, Lang Philipp. Representation of large scale network geometry with realistic apertures determined by mesoscale geomechanical modelling of a natural fracture system. In: *ARMA US Rock Mechanics/Geomechanics Symposium*. ARMA; 2014:ARMA–2014.
120. Stevens Warren Douglas. *RocFall, a Tool for Probabilistic Analysis, Design of Remedial Measures and Prediction of Rockfalls* [PhD thesis]. University of Toronto; 1998.
121. Matas Casado Gerard. *Modelling Fragmentation in Rockfalls* [Ph.d. thesis]. Barcelona, Spain: Universitat Politècnica de Catalunya; 2020.
122. Agliardi Federico, Crosta Giovanni B, Frattini Paolo. Integrating rockfall risk assessment and countermeasure design by 3D modelling techniques. *Nat Hazards Earth Syst Sci*. 2009;9(4):1059–1073.
123. Tavares LM. Energy absorbed in breakage of single particles in drop weight testing. *Miner Eng*. 1999;12(1):43–50.
124. Ruiz-Carulla R, Corominas J, Mavrouli O. Comparison of block size distribution in rockfalls. In: *Landslides and Engineered Slopes. Experience, Theory and Practice*. CRC Press; 2018:1767–1774.